frontiers | Frontiers in Earth Science

ORIGINAL RESEARCH
published: 10 May 2022
doi: 10.3389/feart.2022.859479

Modeling the Deformation Sources in Volcanic Environments Through Multi-Scale Analysis of DInSAR Measurements

Andrea Barone[1], *Maurizio Fedi*[2], *Susi Pepe*[1], *Giuseppe Solaro*[1], *Pietro Tizzani*[1] and *Raffaele Castaldo*[1]*

[1]Institute for Electromagnetic Sensing of the Environment (IREA), National Research Council (CNR), Naples, Italy, [2]Department of Earth, Environmental, and Resources Science (DiSTAR), University of Naples Federico II, Naples, Italy

In this work, we propose a multi-scale approach for modeling the ground deformation field of volcanic sources. The methodology is based on the use of Multiridge and ScalFun methods to analyze the elastic deformation fields by providing source information, such as the depth, the horizontal position, and its morphological features. This strategy is alternative with respect to the classical inverse approaches since it allows overcoming some aspects of the ambiguities related to the interpretation of DInSAR measurements. Indeed, the multi-scale method does not need a priori constraints on the model parameters to achieve an unambiguous solution. First, we argue on the general physical conditions so that the deformation field, generally represented by biharmonic functions, also satisfies Laplace's equation and the law of homogeneity. This occurs in the case of sources with hydrostatic pressure-change embedded in an elastic half-space. In these conditions, the properties of harmonic and homogeneous functions can be employed to model the ground deformation fields using multi-scale procedures. Then, we demonstrate the soundness of the proposed approach through the application of Multiridge and ScalFun methods to synthetic tests. We analyze the fields generated by spherical, pipes- and sills-like sources and consider different model settings, as the layered half-space, the noisy, and the multi-source scenarios. For all these simulations, we achieve unconstrained information related to the source geometry with satisfying accuracy. Finally, in order to show the flexibility of the multi-scale approach in different volcanic environments, we use Multiridge and ScalFun methods for analyzing DInSAR measurements relevant to Uturuncu, Okmok, and Fernandina volcanoes, retrieving information about their volcanic systems. In the first case, we point out a transient source at a depth of 4.5 km b.s.l., which is activated during 2006–2007 together with the stable and well-known Altiplano Puna Magma Body (APMB); in the second one, we retrieve a concentrated body at a depth of 3.1 km b.s.l. during 2003–2004; and in the last case, we interpret the 2013 unrest episode as caused by a pipe-like source located at a depth of 1.7 km b.s.l.

Keywords: multi-scale methods, volcano deformation, source modeling, DInSAR measurements, signal analysis, Uturuncu volcano, Okmok volcano, Fernandina volcano

OPEN ACCESS

Edited by:
Michael Zhdanov,
The University of Utah, United States

Reviewed by:
Oleg E. Melnik,
Lomonosov Moscow State University, Russia
Elizabeth Eiden,
Cornell University, United States

***Correspondence:**
Raffaele Castaldo
castaldo.r@irea.cnr.it

Specialty section:
This article was submitted to Solid Earth Geophysics, a section of the journal Frontiers in Earth Science

Received: *21 January 2022*
Accepted: *25 March 2022*
Published: *10 May 2022*

Citation:
Barone A, Fedi M, Pepe S, Solaro G, Tizzani P and Castaldo R (2022) Modeling the Deformation Sources in Volcanic Environments Through Multi-Scale Analysis of DInSAR Measurements. Front. Earth Sci. 10:859479. doi: 10.3389/feart.2022.859479

1 INTRODUCTION

The volcanic system monitoring is now accomplished by supervising the variation in space and time of different physical dimensions. The development of remote sensing technologies has allowed the ground deformation to be increasingly employed (Dzurisin, 2007). Differential SAR Interferometry (DInSAR) provides spatial and temporal dense measurements, which are suitable for modeling the changes of physical and geometrical parameters of deep and shallow volcanic reservoirs (e.g., Tizzani et al., 2015; Pepe et al., 2019; Castaldo et al., 2021; Rodriguez-Molina et al., 2021).

The most often used strategy to model DInSAR measurements for volcanic monitoring purposes is the parametric inverse modeling (e.g., Battaglia et al., 2013). This approach aims to iteratively identify the parameters of the best-fit Analytical Model (AM) (e.g., Mogi, 1958; Sun, 1969; Geerstma and Van Opstal, 1973; Okada, 1985; McTigue, 1987; Yang and Davis, 1988; Bonaccorso and Davis, 1999; Fialko et al., 2001) through the minimization of a priori selected misfit functions. The AMs expressions are usually retrieved considering the elastic framework (Love, 1906), which is just an approximation of the physical features of volcanic scenarios leading to limitations on model inferences, as well as for the case of elastic half-spaces (e.g., Hickey et al., 2016).

The interpretation of DInSAR measurements is affected by several ambiguities (Dietrick and Decker, 1975; Fialko et al., 2001; Battaglia et al., 2008; Castaldo et al., 2018; Barone et al., 2019). Indeed, this dataset generally provides a discontinuous 2D spatial picture of one or two of the three principal components of the ground deformation field, whose estimates can be also affected by instrumental and/or experimental errors. Therefore, the identification of the representative AM for the analyzed volcanic scenario can be ambiguous, unless the constraining information is available (Dietrick and Decker, 1975). Although several approaches have been proposed to choose the best-fit model (e.g., Battaglia et al., 2008), the use of a wrong representative AM could lead to an incorrect retrieval of its parameters, such as the source depth and/or pressure-change (Fialko et al., 2001). The ambiguities of the inherent nature can also occur. The immediate example is the Mogi model (Mogi, 1958). Specifically, some of its parameters (i.e., the pressure-change ΔP, the radius a, the Poisson coefficient ν, and the shear modulus G) cannot be simultaneously determined, and the most common strategy to find this analytical solution is based on a priori fixing $\nu = 0.25$, searching out the $\Delta P/G$ ratio, and the ΔP has no more physical meaning (Battaglia et al., 2013).

In this framework, we propose an alternative approach for the modeling of DInSAR measurements in volcanic environment, which is an efficient choice over inverse methods, especially in the case of unavailability of constraining information. The methodology requires that the deformation field is expressed by harmonic and homogeneous functions. In particular, the use of multi-scale procedures, such as the Multiridge (Fedi et al., 2009) and ScalFun (Fedi, 2007) methods, is suitable for the retrieval of the source geometrical parameters, or rather the depth, horizontal position, and morphological features (e.g.: Milano et al., 2016; Paoletti et al., 2020). The approach follows the theory of Laplace's equation (Blakely, 1996) and the homogeneity law (Olmsted, 1961), without using the iterative procedures and misfit functions minimization. With regard to the ground deformation field in volcanic environment, Castaldo et al. (2018) and Barone et al. (2019) have already applied Multiridge and Scalfun methods, reducing their validity only to the Mogi source case.

In this article, we generalize the use of multi-scale procedures to the analysis of field generated by point-spherical, pipes- and sills-like ideal sources. We first study the physical conditions such that the biharmonic deformation field (Love, 1906) also satisfies Laplace's equation and the homogeneity laws. This allows us to take advantage of the properties of the harmonic and homogeneous functions to analyze the DInSAR measurements with a multi-scale approach. Then, we show the validity of the proposed conditions by testing the Multiridge and ScalFun methods on different numerical models simulated with the Comsol Multiphysics software (https://www.comsol.com/). We start from the investigation of the geometrical parameters of spherical, pipe- and sill-like sources by analyzing the synthetic vertical and E-W deformation components. Subsequently, we consider the additional model settings as the source embedded in a layered elastic half-space, the case with random noise and the multi-source scenario. We also employ the p-order vertical differentiation of the ground deformation field, which is calculated in the wavenumber-domain for the harmonic functions (Blakely, 1996), pointing out the use of this quantity to perform a higher resolution analysis on the models' geometries.

We apply the Multiridge and ScalFun methods to analyze the deformation patterns retrieved by DInSAR measurements of the three American volcanoes characterized by different geodynamic settings and geochemical features. We study the vertical deformation related to the 2006–2007 uplift event occurred at Uturuncu volcano (Bolivia), retrieved by ENVISAT satellite data, in order to better characterize the transient shallow source with the ScalFun method. At Okmok volcano (Aleutian Islands of Alaska, United States), we analyze the vertical derivatives of descending LOS deformation to assess the scale-invariance *vs.* p of the multi-scale results. To make this, we consider the measurements recorded by 2003–2004 ENVISAT satellite images during the intereruptive stage. Then, we study the horizontal E-W deformation observed at Fernandina volcano (Galapagos Archipelago, Ecuador) recorded by the COSMO-SkyMed satellite during the 2012–2013 unrest episode and provide our interpretation of the volcanic source.

Finally, we discuss our results in relation to the available geological/volcanic models and to the interpretations of geophysical/geodetic data, highlighting the advantages, limitations, and future developments of the proposed multi-scale approach.

2 MATERIALS AND METHODS

The multi-scale approach is based on the analysis of the variation of the ground deformation field at different scales, where the term scale is referred to the distance between the field source and the measurement surface. In this work, we refer to source

distributions that have their support at just one point, known as ideal sources (e.g., Fedi et al., 2015; Vitale and Fedi 2020). Examples related to the volcanic deformations are the point-spherical source (3D concentrated body), whose properties have been already analyzed by Castaldo et al. (2018); the pipe-like source, which generally is nonconcentrated along the z-direction (and concentrated along the x- and y-directions); and the sill-like source that usually is nonconcentrated with respect to the x- and y-directions (and concentrated along the z-direction).

In this section, we treat the general physical conditions so that the biharmonic deformation field satisfies Laplace's equation and the homogeneity law. Then, we describe the used multi-scale methods.

2.1 Harmonic Properties of the Deformation Field

A scalar function ϕ is harmonic if it satisfies Laplace's equation (Blakely, 1996),

$$\nabla^2\phi = \frac{\partial^2\phi}{\partial x^2} + \frac{\partial^2\phi}{\partial y^2} + \frac{\partial^2\phi}{\partial z^2} = 0, \tag{1}$$

and the deformation field $\mathrm{u}(x, y, z) = (u, v, w)$ is also a potential field if any biharmonic component satisfies the following relation (Castaldo et al., 2018):

$$\nabla^2\mathbf{u}(x, y, z) = \begin{pmatrix} \frac{\partial^2 u}{\partial x^2} + \frac{\partial^2 u}{\partial y^2} + \frac{\partial^2 u}{\partial z^2} \\ \frac{\partial^2 v}{\partial x^2} + \frac{\partial^2 v}{\partial y^2} + \frac{\partial^2 v}{\partial z^2} \\ \frac{\partial^2 w}{\partial x^2} + \frac{\partial^2 w}{\partial y^2} + \frac{\partial^2 w}{\partial z^2} \end{pmatrix} = 0. \tag{2}$$

To understand for which conditions **Eq. 2** is satisfied, we consider Navier's relation for equilibrium under surface traction (Love, 1906),

$$\begin{pmatrix} \mu\nabla^2 u + (\lambda+\mu)\frac{\partial}{\partial x}\left(\frac{\partial u}{\partial x} + \frac{\partial v}{\partial y} + \frac{\partial w}{\partial z}\right) \\ \mu\nabla^2 v + (\lambda+\mu)\frac{\partial}{\partial y}\left(\frac{\partial u}{\partial x} + \frac{\partial v}{\partial y} + \frac{\partial w}{\partial z}\right) \\ \mu\nabla^2 w + (\lambda+\mu)\frac{\partial}{\partial z}\left(\frac{\partial u}{\partial x} + \frac{\partial v}{\partial y} + \frac{\partial w}{\partial z}\right) \end{pmatrix} = 0, \tag{3}$$

where, λ and μ are the Lamè's constants. We arrange the terms between the left- and right-hand members,

$$\mu\nabla^2\mathbf{u} = \begin{pmatrix} -(\lambda+\mu)\frac{\partial}{\partial x}\left(\frac{\partial u}{\partial x} + \frac{\partial v}{\partial y} + \frac{\partial w}{\partial z}\right) \\ -(\lambda+\mu)\frac{\partial}{\partial y}\left(\frac{\partial u}{\partial x} + \frac{\partial v}{\partial y} + \frac{\partial w}{\partial z}\right) \\ -(\lambda+\mu)\frac{\partial}{\partial z}\left(\frac{\partial u}{\partial x} + \frac{\partial v}{\partial y} + \frac{\partial w}{\partial z}\right) \end{pmatrix}, \tag{4}$$

and we divide both the members by μ to get:

$$\nabla^2\mathbf{u} = \begin{pmatrix} -\left(1+\frac{\lambda}{\mu}\right)\frac{\partial}{\partial x}\left(\frac{\partial u}{\partial x} + \frac{\partial v}{\partial y} + \frac{\partial w}{\partial z}\right) \\ -\left(1+\frac{\lambda}{\mu}\right)\frac{\partial}{\partial y}\left(\frac{\partial u}{\partial x} + \frac{\partial v}{\partial y} + \frac{\partial w}{\partial z}\right) \\ -\left(1+\frac{\lambda}{\mu}\right)\frac{\partial}{\partial z}\left(\frac{\partial u}{\partial x} + \frac{\partial v}{\partial y} + \frac{\partial w}{\partial z}\right) \end{pmatrix}. \tag{5}$$

Therefore, **u** satisfies Laplace's equation if:

$$\begin{pmatrix} \left(1+\frac{\lambda}{\mu}\right)\frac{\partial}{\partial x}\left(\frac{\partial u}{\partial x} + \frac{\partial v}{\partial y} + \frac{\partial w}{\partial z}\right) \\ \left(1+\frac{\lambda}{\mu}\right)\frac{\partial}{\partial y}\left(\frac{\partial u}{\partial x} + \frac{\partial v}{\partial y} + \frac{\partial w}{\partial z}\right) \\ \left(1+\frac{\lambda}{\mu}\right)\frac{\partial}{\partial z}\left(\frac{\partial u}{\partial x} + \frac{\partial v}{\partial y} + \frac{\partial w}{\partial z}\right) \end{pmatrix} = 0. \tag{6}$$

At this stage, we consider the strain-stress relations expressed by Hooke's Law (Sadd, 2005),

$$\begin{aligned} \frac{\partial u}{\partial x} &= \frac{1}{E}\left(\sigma_{xx} - \nu\sigma_{yy} - \nu\sigma_{zz}\right) \\ \frac{\partial v}{\partial y} &= \frac{1}{E}\left(\sigma_{yy} - \nu\sigma_{zz} - \nu\sigma_{xx}\right) \\ \frac{\partial w}{\partial z} &= \frac{1}{E}\left(\sigma_{zz} - \nu\sigma_{xx} - \nu\sigma_{yy}\right), \end{aligned} \tag{7}$$

and, by substituting them into **Eq. 6**,

$$\begin{pmatrix} \left(1+\frac{\lambda}{\mu}\right)\frac{\partial}{\partial x}\frac{1}{E}\left(\sigma_{xx} - \nu\sigma_{yy} - \nu\sigma_{zz} + \sigma_{yy} - \nu\sigma_{zz} - \nu\sigma_{xx} + \sigma_{zz} - \nu\sigma_{xx} - \nu\sigma_{yy}\right) \\ \left(1+\frac{\lambda}{\mu}\right)\frac{\partial}{\partial y}\frac{1}{E}\left(\sigma_{xx} - \nu\sigma_{yy} - \nu\sigma_{zz} + \sigma_{yy} - \nu\sigma_{zz} - \nu\sigma_{xx} + \sigma_{zz} - \nu\sigma_{xx} - \nu\sigma_{yy}\right) \\ \left(1+\frac{\lambda}{\mu}\right)\frac{\partial}{\partial z}\frac{1}{E}\left(\sigma_{xx} - \nu\sigma_{yy} - \nu\sigma_{zz} + \sigma_{yy} - \nu\sigma_{zz} - \nu\sigma_{xx} + \sigma_{zz} - \nu\sigma_{xx} - \nu\sigma_{yy}\right) \end{pmatrix} = 0, \tag{8}$$

we get:

$$\left(1+\frac{\lambda}{\mu}\right)\nabla\left(\frac{\sigma_{xx}}{E} + \frac{\sigma_{yy}}{E} + \frac{\sigma_{zz}}{E}\right) - 2\nabla\left(\frac{\nu\sigma_{xx}}{E} + \frac{\nu\sigma_{yy}}{E} + \frac{\nu\sigma_{zz}}{E}\right) = 0, \tag{9}$$

that is

$$\frac{1}{1-2\nu}\nabla\left(\frac{\sigma_{kk}}{E}\right) - 2\nabla\left(\frac{\nu\sigma_{kk}}{E}\right) = 0, \tag{10}$$

where, $E = \frac{\mu(3\lambda+2\mu)}{\lambda+\mu}$ is Young's modulus, $\nu = \frac{\lambda}{2(\lambda+\mu)}$ is Poisson's coefficient, and $\sigma_{kk} = \sigma_{xx} + \sigma_{yy} + \sigma_{zz}$. **Eq. 10** is verified if ν is constant and $\nabla\left(\frac{\sigma_{kk}}{E}\right) = 0$. We note that σ_{kk} already depends on E and ν (Sadd, 2005), therefore, the deformation field satisfies Laplace's **Eq. 2** when:

$$\nabla\sigma_{kk} = 0. \tag{11}$$

In the framework of deforming volcanic bodies, **Eq. 11** is always satisfied for a hydrostatic pressure-change within the source embedded in a homogeneous elastic half-space.

The harmonic functions enjoy two crucial field transformations in the wavenumber domain: the upward continuation and the vertical differentiation (Blakely, 1996). The upward continuation is used to form the multi-scale deformation 3D spatial dataset starting from the 2D spatial measured data (i.e., DInSAR measurements). The upward continued field f_c is just the deformation field that would have been generated by the same source of the measured data f and upwardly extending the medium by the amount of continuation Δz_i (Castaldo et al., 2018). Specifically, we retrieve f_c by antitransforming into the space-domain the following relation (Blakely, 1996):

$$\mathcal{F}[f_c] = \mathcal{F}[f]e^{-\Delta z_i|k|}, \tag{12}$$

where, $\mathcal{F}[f_c]$ and $\mathcal{F}[f]$ are the Fourier transforms of f_c and f, respectively, and k is the wavenumber.

The vertical differentiation of order p of the ground deformation field $\partial^p f/\partial z^p$ enhances the high-wavenumber contributions of the signal, so as to better characterize the shallowest sources and/or their shallowest parts (Barone et al., 2019). Also, we provide $\partial^p f/\partial z^p$ by antitransforming the following relation (Blakely, 1996):

$$\mathcal{F}\left[\frac{\partial^p f}{\partial z^p}\right] = |k|^p \mathcal{F}[f]. \tag{13}$$

2.1.1 Multiridge Method

The method is based on the analysis of the so-called ridges, i.e., the lines formed by joining the zeros of the field and its derivatives at several scales (multiridge subset). The ridges intersection provides information on the field source position (Fedi et al., 2009).

Since the method is based on a level-to-level approach (Fedi et al., 2009) and the measurement surface of the DInSAR data (topography) is uneven, the first step is the upward continuation from the uneven surface to a flat one, called draped-to-flat continuation. We numerically generate a ground deformation field that could have been measured as relocated onto a constant measurements level (Castaldo et al., 2018). This is performed in the continuous wavelet transform (CWT) domain (Ridsdill-Smith and Dentith, 1999). A 3D spatial multi-scale dataset is then generated through the flat-to-flat upward continuation (Blakely, 1996) to a set of different scales, in agreement with **Eq. 12**.

The second step is based on searching out the zeros of the vertical (multiridge subset I) and horizontal (multiridge subset II) derivatives of the deformation field at different scales z. Consider the vertical deformation produced by a simple Mogi source (Mogi, 1958),

$$w = a^3 \Delta P \frac{1-\nu}{G} \frac{z - z_0}{|\mathbf{r}|^3}, \tag{14}$$

where $|\mathbf{r}| = \sqrt{(x-x_0)^2 + (y-y_0)^2 + (z-z_0)^2}$; without the loss of generality with regard to the cross-section $y = y_0$ and the case $a^3 \Delta P \frac{1-\nu}{G} = 1$, we calculate the zeros of the horizontal and vertical derivatives of **Eq. 14**:

$$\frac{\partial w}{\partial x} = -\frac{3(x-x_0)(z-z_0)}{|\mathbf{r}|^5} = 0, \tag{15}$$

$$\frac{\partial w}{\partial z} = \frac{1}{|\mathbf{r}|^3} - \frac{3(z-z_0)^2}{|\mathbf{r}|^5} = 0. \tag{16}$$

The following ridges equations are then retrieved since $z \neq z_0$:

$$x = x_0, \tag{17}$$

$$x - x_0 = 2(z - z_0), \tag{18}$$

$$x - x_0 = -2(z - z_0), \tag{19}$$

Equations 17–19 are simple straight lines, which intersect each other at the source's center (x_0, z_0).

In the third step, the best-fit linear regressions of the multiridge subsets allow the identification of the ridges, and the retrieval of their intersections gives back the source position. **Equations 14–19** show that ridges intersections occur at the body center for the point-spherical sources. However, ridges intersections can indicate the different features of the analyzed body, such as the top or the boundaries of the pipe- and sill-like sources.

In the last step, we evaluate the uncertainties of the estimated parameters, as follows: (i) for each multiridge subset, we calculate the linear regression R^2 coefficient, which represents a statistical measure of the fitted regression line (ridges); (ii) by considering 95% of confidence interval of the best-fit linear regression, we retrieve the bounds parameters for each ridge (intercept and slope constants); (iii) we draw the best-fit and bounds ridges; (iv) identifying their multiple intersections, which represent the source parameters (i.e., East and North positions, depth) and their uncertainties.

2.2 Homogeneity Properties of Deformation Field

A homogeneous function f satisfies the following scaling law in the region R:

$$f(tx, ty, tz) = t^n f(x, y, z), \tag{20}$$

where, $t > 0$ and $n \in \mathbb{R}$ is the homogeneity degree of f. When f is continuously differentiable, Euler's theorem describes the homogeneity, as follows (e.g., Olmsted, 1961; Vitale and Fedi, 2020):

$$\nabla f(\mathbf{r}) \cdot (\mathbf{r} - \mathbf{r}_0) = -nf(\mathbf{r}), \tag{21}$$

where, $\mathbf{r}_0$ represents the position of the field source.

n often expresses the falloff rate of the anomaly with the scale. It is an integer and constant for the fields generated by ideal sources (e.g., Fedi et al., 2015). Castaldo et al. (2018) have shown that a point-spherical source with a hydrostatic ΔP (i.e., the Mogi model) generates a homogeneous ground deformation field with $n = -2$.

Accordingly, $-2 \le n \le 1$ characterize the fields generated from the 3D concentrated to nonconcentrated sources, respectively.

The homogeneity properties reflect the type of field source. In the case of the harmonic deformation field, which is the first-order derivative of a Newtonian potential, we get the homogeneity degree of the source n_s,

$$n_s = n - 1, \tag{22}$$

and, in turn, the structural index of the source N (e.g., Fedi, 2007):

$$N = -n_s. \tag{23}$$

N takes on an important meaning since it represents a source parameter characterizing its geometry. Following Fedi et al. (2015), we define N as an integer number varying from 0 to 3 going from a 3D nonconcentrated to concentrated sources. For example, $N \sim 3$ characterizes a point-spherical source or mathematically equivalent body concentrated in its center; $N \sim 2$ indicates source distribution supported on its top, as the pipe-like one, and finally, $N \sim 1$ is related to sill- and dike-like sources, for which their edges are representative of the source distribution.

2.2.1 Scalfun Method

This method is based on the properties of the scaling function, which is particularly suited to analyze a multi-scale dataset. Let us consider the p^{th}-order vertical derivative of a given component f of the deformation field at (x_0, y_0, z_0) and at the multiridge subset II. In this case, we define the scaling function τ_p as (Fedi, 2007):

$$\tau_p = \frac{\partial \log f_p}{\partial \log z} = -(p-n)\frac{z}{z - z_0}, \tag{24}$$

where n is the homogeneity degree of the deformation field and z is the scale. By putting $z = 1/q$, τ_p becomes

$$\tau_p(q) = -\frac{(p-n)}{1 - z_0 q}, \tag{25}$$

which means that when $q \to 0$, $\tau_p(q)$ tends to $-(p-n)$.

Therefore, by using in **Eq. 25** the estimated depth z_0 with the Multiridge method, we evaluate τ_p through the plot diagram vs. q (Fedi, 2007) and, since p and q are known, we retrieve n. **Equations 22**, **23** allow to find n_s and N, which yields information about the source geometry.

The uncertainties related to the estimates of $\tau_p(q)$ are evaluated by substituting the bounds values of z_0 into **Eq. 25**, retrieved as described in **Section 2.1.1**.

3 RESULTS

3.1 Application to Synthetic Deformation Fields

We show the validity of the multi-scale approach by applying Multiridge and ScalFun methods to synthetic deformation fields. We simulate both harmonic and nonharmonic fields using a Finite Element (FE) approach (COMSOL Multiphysics software), which allows us to model different scenarios or to accurately reproduce fields satisfying the **Eq. 11** and Laplace's equation (**Eq. 2**).

We consider the simple and geometrically finite sources, characterized by hydrostatic ΔP and embedded in a homogeneous elastic half-space, to model the following cases: (I) the sphere, with radius $r = 0.5$ km, which is the simplest approximation of a magma chamber; (II) the ascent-pipe, here represented by an ellipsoid with semi-axes $r_x = r_y = 0.5$ km and $r_z = 2.5$ km (aspect ratio of the ellipsoid = 0.2); (III) the sill emplacement, here approximated by using a rectangular prism with sides $L_x = L_y = 5$ km and $L_z = 1$ km. Furthermore, we take into account the additional synthetic cases with different model settings: (IV) the layered half-space test, where a sill-like source is embedded in a heterogeneous medium, characterized by three layers with an increasing E distribution vs. depth (2 GPa for the layer 0–1 km, 7 GPa for 1–3 km, and 10 GPa for the last one); (V) the noisy case, where 30% (with respect to the maximum value) of the random noise is added to the latter simulated field (**Supplementary Figure S1**); and (VI) the multi-source scenario, where the over-pressurized spherical and pipe-like sources contribute to the same deformation anomaly. The other FE modeled parameters are reported in **Supplementary Tables S1, S2**.

We start from the analysis of the vertical deformation components ($p = 0$) of the first three cases (**Figures 1A–C**). We calculate the 3D spatial multi-scale datasets by the upward continuation of the deformation fields from 0 to 15 km, with a 0.4 km step, and extract the profile (black dashed lines in **Figures 1A–C**) passing through the maximum value of the anomalies. We use the multiridge subsets (blue and black dots in **Figures 1D–F**) to represent the ridges (red continuous lines in **Figures 1D–F**). For the sphere (I), we note that the ridges intersection indicates a source located at $x = 50$ km and -3 km depth (**Figure 1D**). Instead, for the pipe (II), the ridges above 5 km scale line up along the same straight line of the previous one and the intersection occurs at $x = 50$ km and -2.8 km depth (**Figure 1E**). We observe a similar behavior for the sill (III), where we consider the upward continued field above 8 km scale to retrieve the ridges intersection at the point $x = 50$ km and -3.1 km depth (**Figure 1F**). For these cases, the results of the ScalFun method indicate (**Figures 1G–I**): $\tau \sim -2$ and $n \sim -2$ according to the **Eq. 25**, and $N \sim 3$ for **Eqs 22**, **23**.

We also analyze these cases using the vertical differentiation of the ground deformation field. We calculate the first-order vertical derivatives ($p = 1$) of the deformation field for the sphere (**Figure 2A**) and of the pipe (**Figure 2B**), and the second-order vertical derivatives ($p = 2$) for that of the sill (**Figure 2C**). Then, we create a 3D spatial multi-scale dataset up to 5 km, with a 0.4 km continuation step, and extract the profile (black dashed line in **Figures 2A–C**) passing through the maxima of the vertical derivatives. For the sphere (I), the ridges intersection again occurs at $x = 50$ km and -3 km depth (**Figure 2D**). The ScalFun method indicates (**Figure 2E**): $\tau_1 \sim -3$ and $n \sim -2$ according to **Eq. 25**, and $N \sim 3$ for **Eqs 22**, **23**. For the pipe (II), we achieve two sets of ridges with different intersections, one of which indicates the point with $x = 50$ km and -0.51 km depth, that is near the source top (**Figure 2F**). The

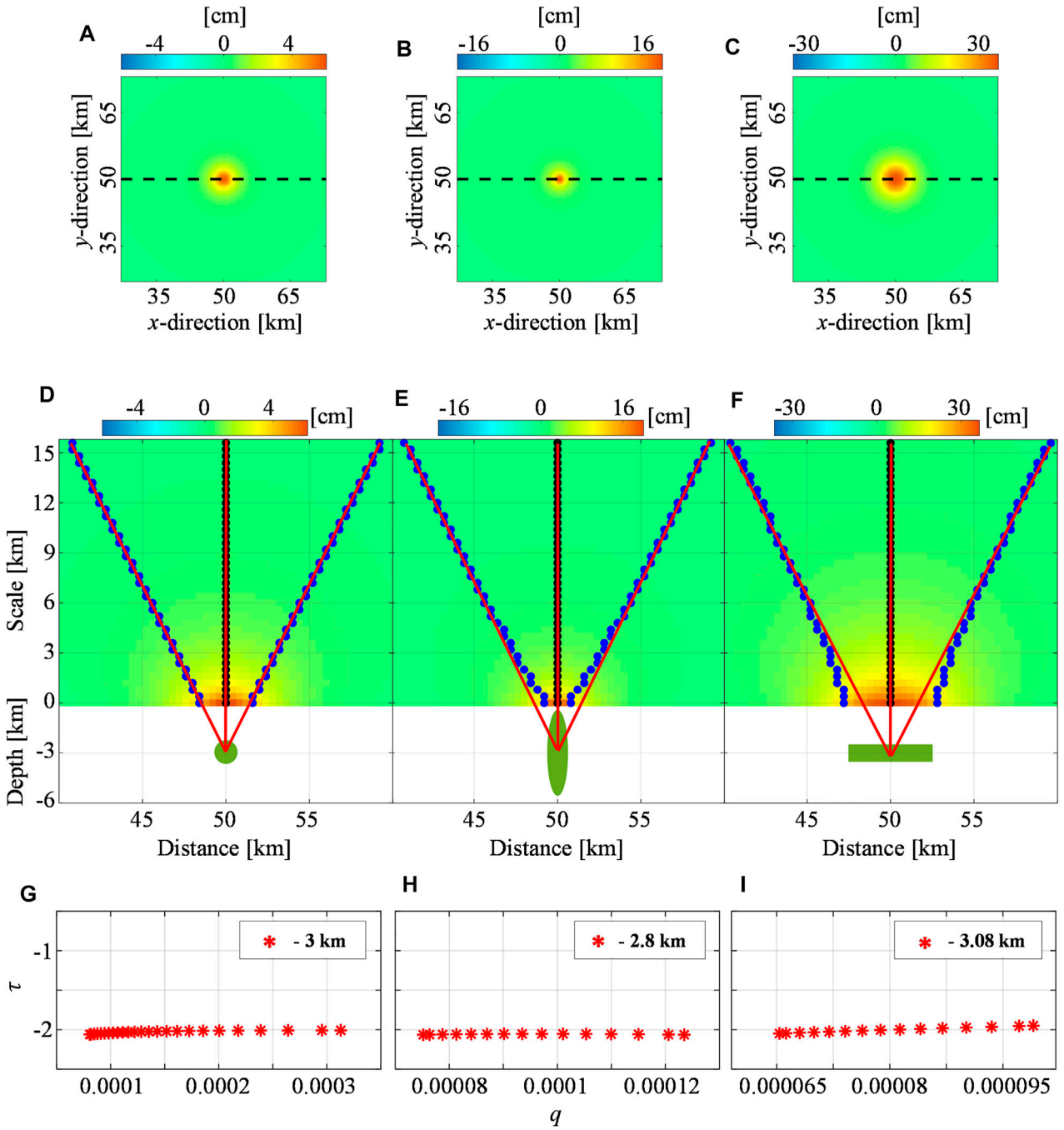

FIGURE 1 | Spherical, pipe-, and sill-like synthetic sources: vertical deformation. Modeled vertical component ($p = 0$) generated by the overpressurized **(A)** spherical, **(B)** pipe-, and **(C)** sill-like sources. The black dashed lines indicate the positions of the analyzed profiles. **(D–F)** The Multiridge method applied to the three cases; vertical deformations are also shown at different scales z; blue and black dots point out the zeros of vertical (subset I) and horizontal (subset II) derivatives of the analyzed dataset, respectively, while the red solid lines represent the best-fit regression lines; the green geometries show the vertical sections of the sources. **(G–I)** The ScalFun method applied to the three cases; red stars indicate $\tau = \partial \log f / \partial \log z$ [-] in function of $q = 1/z$ [km^{-1}] using the source depth retrieved by the Multiridge method, where f are the values of the analyzed vertical component at the subset II.

ScalFun method characterizes this solution with $N \sim 2$, since $\tau_1 \sim -2$ and $n \sim -1$ (**Figure 2G**). Finally, for the sill (III), the ridges converge at two different points with coordinates $(x, z) = (47.6, -2.4)$ km and $(x, z) = (52.4, -2.4)$ km, near the body edges (**Figure 2H**). The ScalFun method characterizes these solutions (**Figure 2I**) with $\tau_2 \sim -2$, $n \sim 0$, and $N \sim 1$.

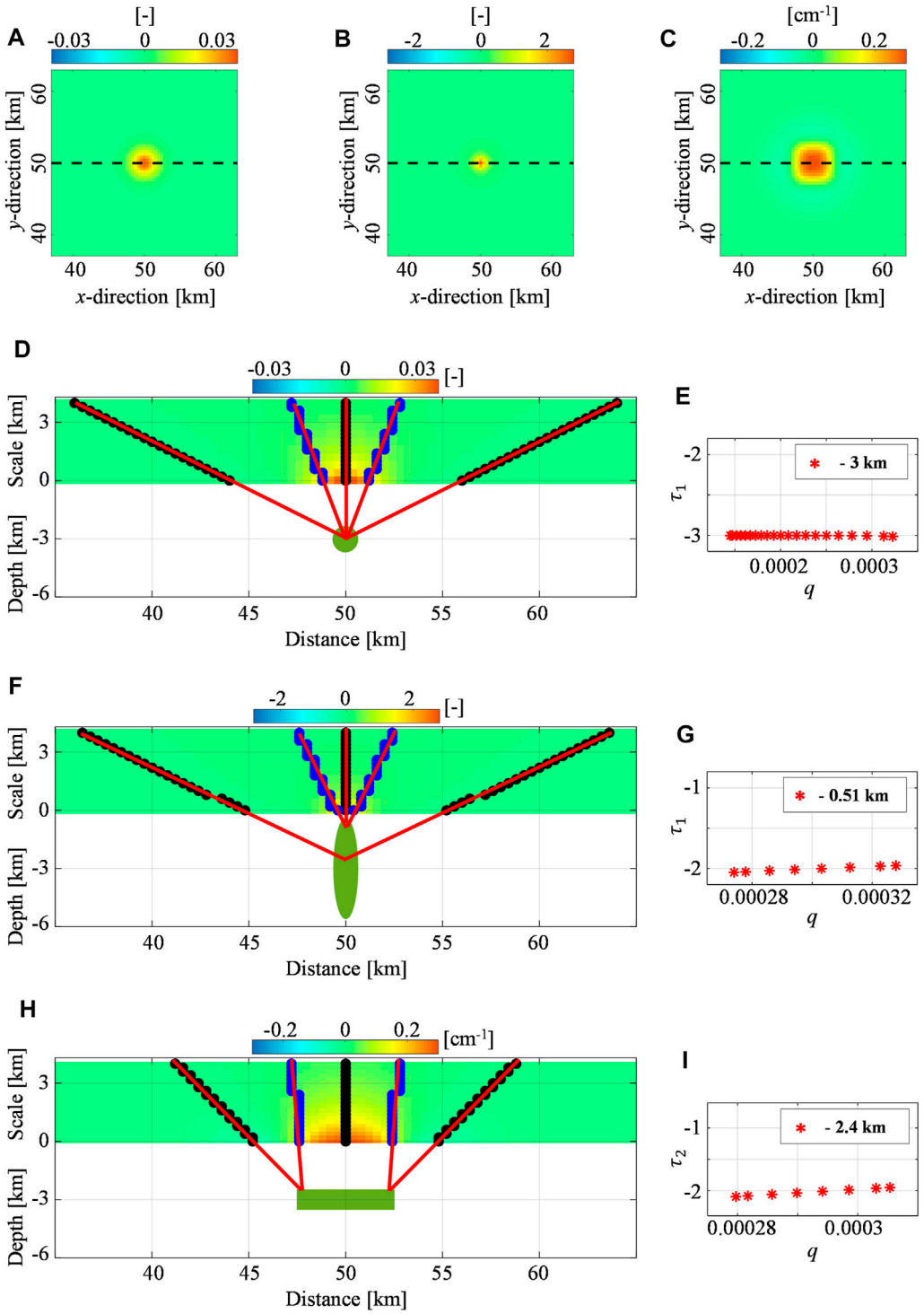

FIGURE 2 | Spherical, pipe-, and sill-like synthetic sources: vertical derivative of the vertical deformation. **(A,B)** First-order (p = 1) and **(C)** second-order (p = 2) vertical derivatives of the modeled vertical component generated by the overpressurized spherical, pipe-, and sill-like sources, respectively. The black dashed lines indicate the positions of the analyzed profiles. The Multiridge and ScalFun methods applied to the **(D,E)** spherical, **(F,G)** pipe-, and **(H,I)** sill-like source cases. Vertical derivatives are also shown at different scales z; blue and black dots point out the zeros of vertical (subset I) and horizontal (subset II) derivatives of the analyzed dataset, respectively, while the red solid lines represent the best-fit regression lines; the green geometries show the vertical sections of the sources; red stars indicate $\tau_p = \partial \log f_p / \partial \log z$ [-] in the function of $q = 1/z$ [km^{-1}] using the source depth retrieved by the Multiridge method, where f_p are the values of the analyzed dataset at subset II.

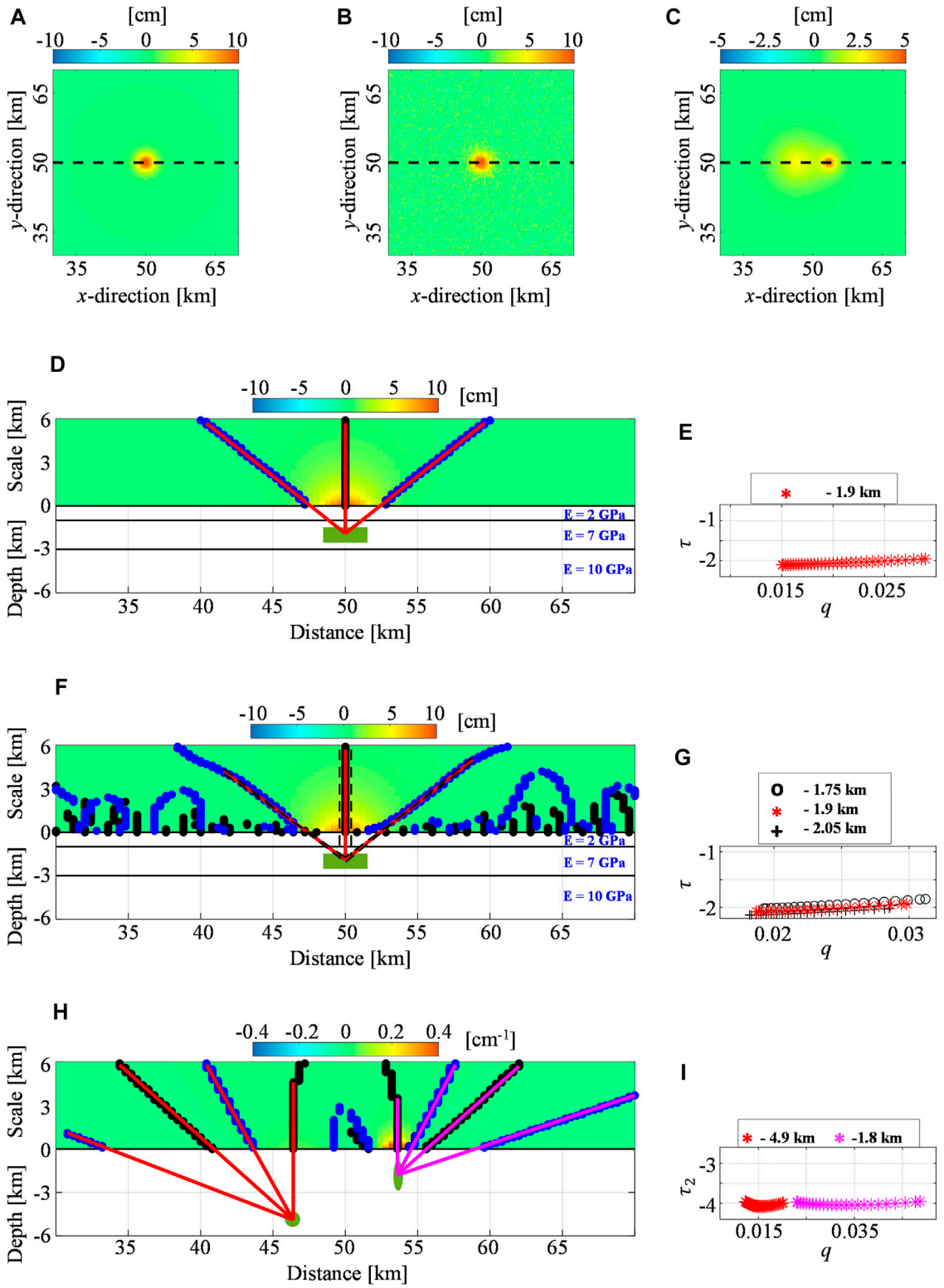

FIGURE 3 | Layered half-space, noisy, and multi-source synthetic cases. The modeled vertical component related to the **(A)** layered half-space case, **(B)** noisy test, and **(C)** multi-source scenario. The black dashed lines indicate the positions of the analyzed profiles. The Multiridge and ScalFun methods applied to the **(D,E)** layered half-space case, **(F,G)** noisy test, and **(H,I)** multi-source scenario. Vertical deformations and vertical derivatives are also shown at different scales *z*; blue and black dots point out the zeros of vertical (subset I) and horizontal (subset II) derivatives of the analyzed dataset, respectively, while the red/magenta solid and black dashed lines

(*Continued*)

FIGURE 3 | represent the best-fit regression lines and the linear regression boundary solutions, respectively; black solid lines describe the layered setting and Young's modulus is also shown. The green geometries show the vertical sections of the sources; red stars and black crosses/circles indicate $\tau_p = \partial \log f_p / \partial \log z$ [-] in function of $q = 1/z$ [km^{-1}] using the best-fit and boundary depth solutions retrieved by the Multiridge method, respectively, where f_p are the values of the analyzed dataset at subset II.

TABLE 1 | Summary of application to synthetic cases. *w*, *u*, and *p* are related to the analyzed dataset and stand for the vertical, EW components, and the order of the analyzed vertical derivative of the synthetic ground deformation field, respectively. *x*, *z*, and *N* indicate the horizontal coordinates, the depth, and the structural index parameters, while the subscripts c and t/b are related to the center and top/boundaries of the source, respectively.

Test case	Expected results	Analyzed dataset	Retrieved results					
			x_c (km)	z_c (km)	N_c	$x_{t/b}$ (km)	$z_{t/b}$ (km)	$N_{t/b}$
Single	*xc* = 50 km	*w*	50	3	3	–	–	–
		u	50	3.03	3	–	–	–
Source	*zc* =–3 km	*p* = 1 (*w*)	50	3	3	–	–	–
SPHERE	*N* = 3	*p* = 1 (*u*)	50	3	3	–	–	–
Single	*xc* = 50 km	*w*	50	2.8	3	–	–	–
		u	50	2.95	3	–	–	–
Source	*zc* =–3 km	*p* = 1 (*w*)	–	–	–	50	0.51	2
PIPE	*N* = 3	*p* = 2 (*u*)	–	–	–	50	0.6	2
Single	*xc* = 50 km	*w*	50	3.08	3	–	–	3
		u	50	3.0	3	–	–	3
Source	*zc* =–3 km	*p* = 2 (*w*)	–	–	–	(47.6,52.4)	2.4	1
SILL	*N* = 3	*p* = 2 (*u*)	–	–	–	(47.6,52.4)	2.4	1
Layered Half-space SILL	*xc* = 50 km *zc* =–2 km *N* = 3	*w*	50	1.9	3	–	–	–
Noisy test SILL	*xc* = 50 km *zc* =–2 km *N* = 3	*w*	50	1.9	3	–	–	–
Multi-source	*xc* = 46.5 km *zc* =–5 km *N* = 3	*p* = 2 (*w*)	46.4	4.9	3	–	–	–
SPHERE and PIPE	*xc* = 53.5 km *zc* =–2 km *N* = 3		53.6	1.8	3	–	–	–

Similar considerations occur by analyzing the E-W deformation components and their vertical derivatives, whose results are reported in **Supplementary Figures S2, S3**.

For what concern the layered scenario (IV), we analyze the vertical component (**Figure 3A**) of the deformation ($p = 0$) and observe the ridges intersection at $x = 50$ km and -1.9 km depth (**Figure 3D**). The ScalFun method indicates (**Figure 3E**): $\tau \sim -2$ and $n \sim -2$ according to **Eq. 25**, and $N \sim 3$ for **Eqs 22**, **23**. We still analyze the vertical deformation (**Figure 3B**) component ($p = 0$) modeled for the noisy test (V) and retrieve a single intersection at $x = 50 \pm 0.4$ km with -1.9 ± 0.15 km depth (**Figure 3F**). Also, the ScalFun method characterizes this solution with $N \sim 3$, since $\tau \sim -2$ and $n \sim -2$ (**Figure 3G**). Finally, for the multisource case (VI), we analyze the second order vertical derivative ($p = 2$) of the vertical deformation (**Figure 3C**) and retrieve two sets of ridges converging at two different points with coordinates $(x, z) = (46.4, -4.9)$ km and $(x, z) = (53.6, -1.8)$ km (**Figure 3H**). The ScalFun method characterizes both the solutions (**Figure 3I**) with $\tau_2 \sim -4$, $n \sim -2$, and $N \sim 3$.

A summary of the performed tests is reported in **Table 1**.

3.2 Application to Real Cases

3.2.1 Uturuncu Volcano

Uturuncu volcano (**Figure 4**) lies on a large continental crustal magma body and its magmatism is the result of eastwards subduction of the Nazca oceanic plate beneath the South American continent (de Silva and Gosnold, 2007). It is a long-dormant effusive stratovolcano located at almost the center of the largest up doming zone on the Earth, the Altiplano-Puna Volcanic Complex (APVC) (Gottsmann et al., 2017). This site has been studied within the interdisciplinary PLUTONS project (Pritchard et al., 2018) through the analysis of different datasets. Both the geophysical and geochemical studies have highlighted the deep Altiplano-Puna Magma Body (APMB) (Allmendinger et al., 1997; Schmitz et al., 1997; Schilling et al., 1997; Chmielowski et al., 1999; Zandt et al., 2003; Sparks et al., 2008; del Potro et al., 2013; Ward et al., 2014; Comeau et al., 2015; Comeau et al., 2016; Perkins et al., 2016; Kukarina et al., 2017; Ward et al., 2017; McFarlin et al., 2017), whose role in producing the observed multi-decade decimeter-scale deformation signal is surely crucial. Indeed, several authors have interpreted InSAR measurements by modeling the deformation field through a deep source with different geometry associated to the APMB (Pritchard and Simons, 2002; Pritchard and Simons, 2004; Fialko and Pearse, 2012; Henderson and Pritchard, 2013; Hickey et al., 2013; Walter and Motagh, 2014; Gottsmann et al., 2017; Henderson and Pritchard, 2017; Barone et al., 2019). In addition to this, geochemical, petrological, and geophysical analyses have also supported the existence of shallow magma storage (Sparks et al., 2008; Jay et al., 2012; Muir et al., 2014; Alvizuri and

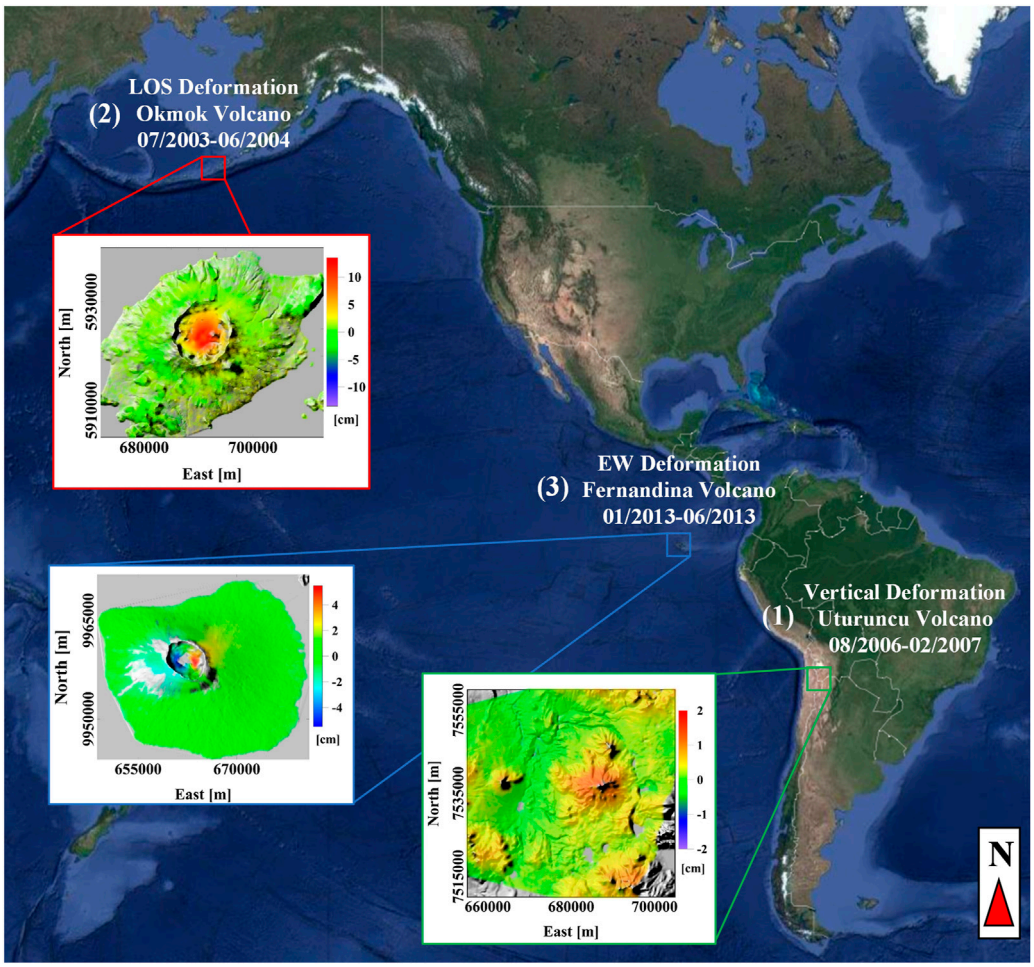

FIGURE 4 | Unrest volcanoes case studies. The geographic location and DInSAR measurements of the three volcanic sites considered for the application of the Multiridge and ScalFun methods: (1) Uturuncu volcano and the related cumulative vertical deformation recorded between 08/2006 and 02/2007 (dataset from Barone et al., 2019); (2) Okmok volcano and the related LOS deformation recorded in the time interval 07/2003–06/2004 along descending orbit (dataset from Castaldo et al., 2018); and (3) Fernandina volcano and the related cumulative E-W deformation recorded between 01/2013 and 06/2013 (dataset from Pepe et al., 2017).

Tape, 2016; Comeau et al., 2016), despite the condition that related deformation source may have transient nature (Lau et al., 2018). Accordingly, Barone et al. (2019) have analyzed the 2005–2008 ENVISAT DInSAR time-series through a combination of the cross-correlation analysis and Multiridge method to delineate a multisource scenario, consisting of the deep APMB source and a transient shallow one.

In this work, we use the multi-scale approach to analyze the same dataset (**Figure 4**) of Barone et al. (2019) related to the August 2006 - February 2007 unrest by focusing our study on the characterization of the shallow transient source through the use of the ScalFun method. We consider the cumulative vertical deformation ($p = 0$) recorded during this unrest and calculate a regular grid (natural neighbor interpolator) with 200 m sampling step. The 6.5 km a.s.l. draped-to-flat continued field is shown in **Figure 5A**.

In **Figure 6**, we show the results of our application by considering the E-W and N-S profiles (black dashed lines in **Figure 5A**). Specifically, we analyze the 3D spatial multi-scale dataset up to the ≈ 12 km scale and we find the two-ridges intersection along both the sections by inferring -4.5 ± 0.4 km b.s.l. depth to the source with an UTM coordinate of 688,000 ± 100 m E and 7538400 ± 100 m N (**Figures 6A,B**). The ScalFun method allows the characterization of this solution with $N \sim 3$ since $\tau \sim -2$ and $n \sim -2$ (**Figures 6C,D**), according to **Eqs 22**, **23**, **25** and $p = 0$.

3.2.2 Okmok Volcano

Okmok volcano (**Figure 4**) is located on the oceanic crust as the results of the subduction between the Pacific and North American plates. It is an active basaltic shield volcano located at the north-eastern part of the Umnak Island in Alaska, US (Finney et al., 2008). For this site, the deformation data has provided consistent information through the source modeling of the unrest phenomena that occurred before the 2008 eruption. Several

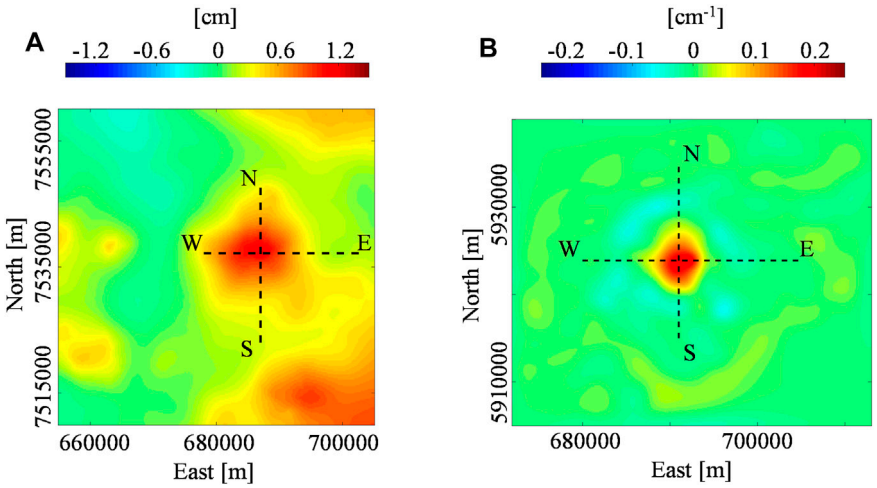

FIGURE 5 | Deformation maps at Uturuncu and Okmok volcano. **(A)** Uturuncu volcano: cumulative vertical deformation referred to the 6.5 km a.s.l. scale and recorded in the time interval 08/2006–02/2007. **(B)** Okmok volcano: second-order vertical derivative of the LOS deformation referred to the 2 km a.s.l. scale and recorded in the time interval 07/2003–06/2004 along the descending orbit.

authors have used different approaches and modeled the deformation source through spherical geometries and the Mogi source at a depth of 3–4 km b.s.l. (e.g.: Lu et al., 2005; Masterlark et al., 2010; Biggs et al., 2010; Masterlark et al., 2012; Castaldo et al., 2018; Xue et al., 2020). In particular, Castaldo et al. (2018) have already considered the multi-scale approach to study the LOS deformation acquired by the ENVISAT satellite along the descending orbit during the period July 2003—June 2004 by retrieving a Mogi source at −3.4 km b.s.l.

In this framework, we consider the dataset presented by Castaldo et al. (2018) and apply the vertical differentiation operator. We calculate a regular grid (natural neighbor interpolator) with 100 m sampling step and compute the second-order ($p = 2$) vertical derivative (**Figure 5B**) of the draped-to-flat continued field to 2 km a.s.l. scale. We analyze the 3D spatial multi-scale dataset with the Multiridge and ScalFun methods, starting from the 4 km a.s.l scale.

In **Figure 7**, we show the results along the E-W and N-S sections (black dashed lines in **Figure 5B**) of a 3D spatial multi-scale dataset up to the 12 km a.s.l. scale. We identify the ridges intersection at −3.1 ± 0.4 km b.s.l. depth with UTM coordinate at 691000 ± 100 m E and 5924000 ± 200 m N (**Figures 7A,B**). This solution is characterized by the ScalFun method with $N \sim 3$, since $\tau_2 \sim -4$ and $n \sim -2$, according to **Eqs 22**, **23**, **25** and $p = 2$ (**Figures 7C,D**).

3.2.3 Fernandina Volcano

Fernandina Volcano, located on the Nazca Plate (**Figure 4**), is one of the most active centers of the Galapagos Archipelago that mainly erupts tholeiitic basalt (McBirney and Williams, 1969). Several authors have used both the DInSAR and GPS measurements for modeling its volcanic system using the source mechanism as sills and dikes (Jonsson et al., 1999; Chadwick et al., 2011; Bagnardi and Amelung, 2012). The most suitable deformation model seems to be a shallow dipping sill intrusion at about 1 km b.s.l. (Bagnardi and Amelung, 2012). This model is able to match well with the volcanic and structural features as the change of the eruptive fissures orientations from sub-horizontal to vertical, which occurs if the feeding of the circumferential fissures is near the caldera margin or when a twist feeds fissure eruptions on the flanks (Bagnardi et al., 2013; Corbi et al., 2015). Moreover, a deep magmatic reservoir is also pointed out at about 5 km b.s.l. and it is hydraulically connected with the shallower one (Bagnardi and Amelung, 2012). Indeed, Pepe et al. (2017) have proposed a pipe-like source with a depth of 1.5 km b.s.l. to model the 2012–2013 unrest event. This result has been associated with mechanisms of magma migration from the deep cumulate complex to shallow the volcanic reservoirs within the same magmatic feeding system.

In this scenario, we start from the same processed SAR images (COSMO-SkyMed satellite images) by Pepe et al. (2017) and apply the multi-scale approach. The dataset (**Figures 8A,B**) shows an unrest with the vertical and E-W mean velocity of ≈ 13 and ≈ 8 cm/yr, respectively, throughout the 2012–2013 time interval. From the time-series (**Figures 8C,D**), we select January 2013–June 2013 interval, in which the deformation shows the most significant velocity (vertical black continuous lines in **Figures 8C,D**). Both the components have the similar order of accuracy (Pepe et al., 2017) and, specifically, we consider the cumulative deformation of the E-W component. We perform the gridding operation by using the natural neighbor interpolator with 100 m of the sampling step and apply the draped-to-flat upward continuation to 1.5 km a.s.l. scale (**Figure 8E**). We select three profiles (black dashed lines in **Figure 8E**) for the analysis of the first-order ($p = 1$), second-order ($p = 2$), and third-order ($p = 3$) vertical derivatives.

We make some comments by considering the CD profile (black dashed lines in **Figure 8E**), which is E-W oriented. The application of the Multiridge method to the first-order vertical derivative shows that the ridges intersect at the point coordinates

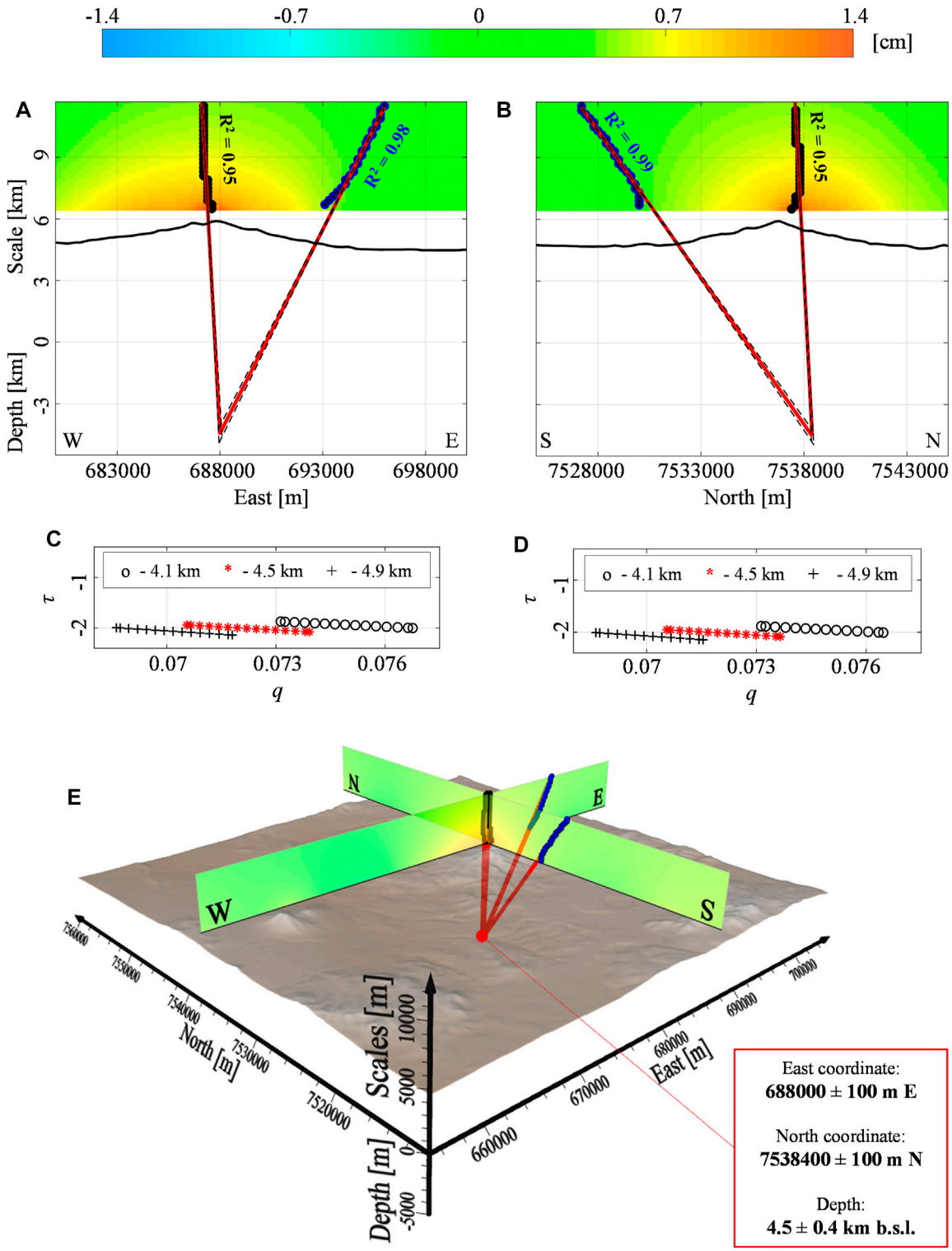

FIGURE 6 | Uturuncu volcano: vertical deformation. The Multiridge method along the **(A)** W-E and **(B)** S-N oriented sections of the vertical component ($p = 0$) recorded in the time interval 08/2006–02/2007; blue and black dots point out the zeros of vertical (subset I) and horizontal (subset II) derivatives of the analyzed vertical deformation, respectively; vertical deformations are also shown at different scales z; red solid and black dashed lines represent the best-fit regression lines and the linear regression boundary solutions, respectively. For each regression line, we indicate the R^2 coefficient; black solid lines are the volcano topography. **(C,D)** The ScalFun method along the two sections; red stars and black crosses and circles indicate $\tau = \partial \log f / \partial \log z$ [-] in function of $q = 1/z$ [km^{-1}] calculated using the best-fit and boundary depth solutions retrieved by the Multiridge method, respectively, where f are the values of the analyzed vertical deformation at the subset II. **(E)** Summary of the results. The topography is also shown; the red circle indicates the source location. UTM-WGS84 projection zone: 19S.

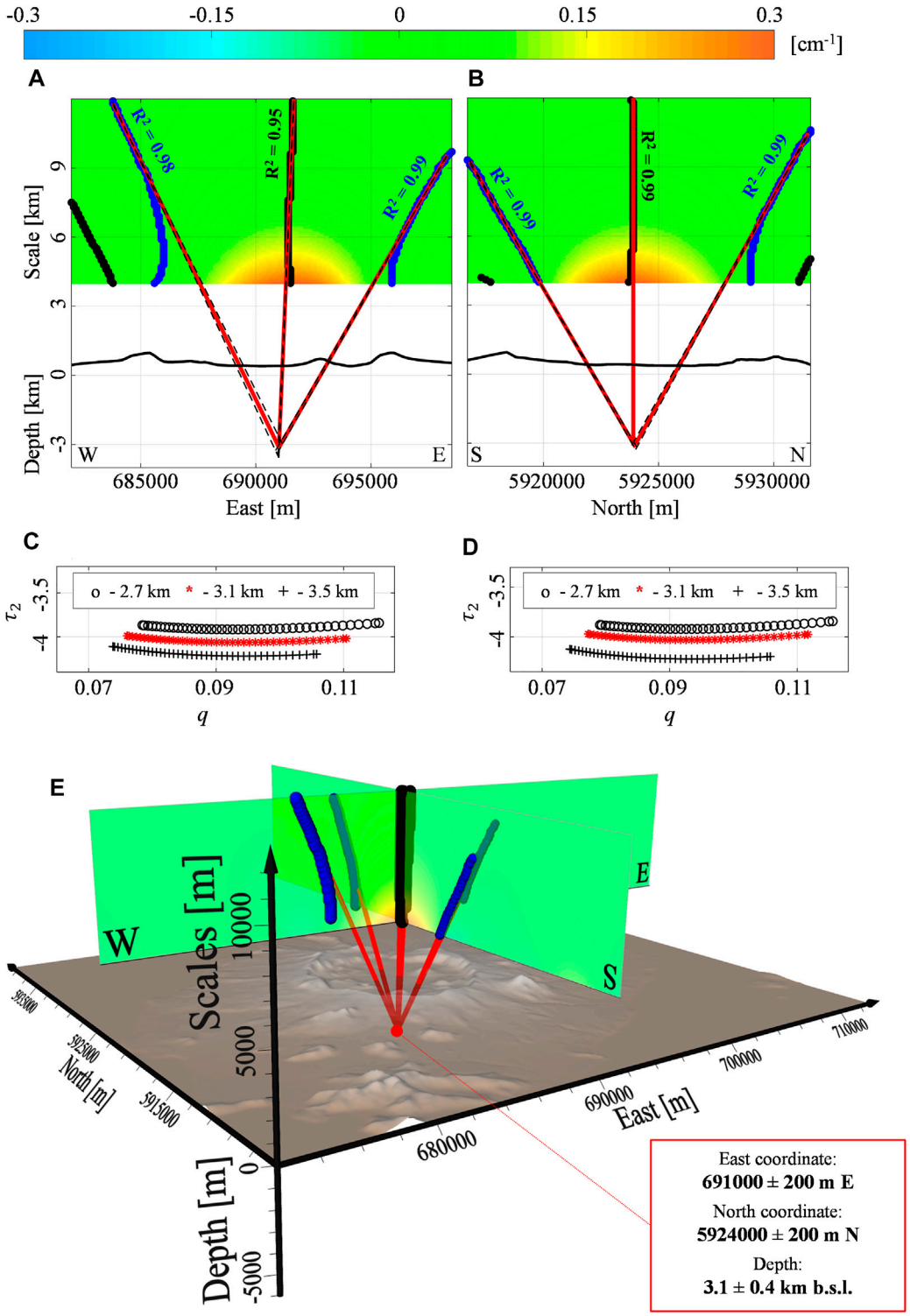

FIGURE 7 | Okmok volcano: second-order vertical derivative of LOS deformation. The Multiridge method along the **(A)** W-E and **(B)** S-N oriented sections of the second-order ($p = 2$) vertical derivative of the LOS deformation recorded in the time interval 07/2003–06/2004; blue and black dots point out the zeros of vertical (subset I) and horizontal (subset II) derivatives of the analyzed dataset, respectively. Vertical derivatives are also shown at different scales z; red solid and black dashed lines represent the best-fit regression lines and the linear regression boundary solutions, respectively. For each regression line, we indicate the R^2 coefficient; black solid lines are the topography. **(C,D)** The ScalFun method along the two sections; red stars and black crosses and circles indicate $\tau_2 = \partial \log f_2 / \partial \log z$ [-] in function of $q = 1/z$ [km^{-1}] calculated using the best-fit and boundary depth solutions retrieved by the Multiridge method, respectively, where f_2 are the values of the analyzed second-order vertical derivative at subset II. **(E)** Summary of the results. The topography is also shown. The red circle indicates the source location. UTM-WGS84 projection zone: 2N.

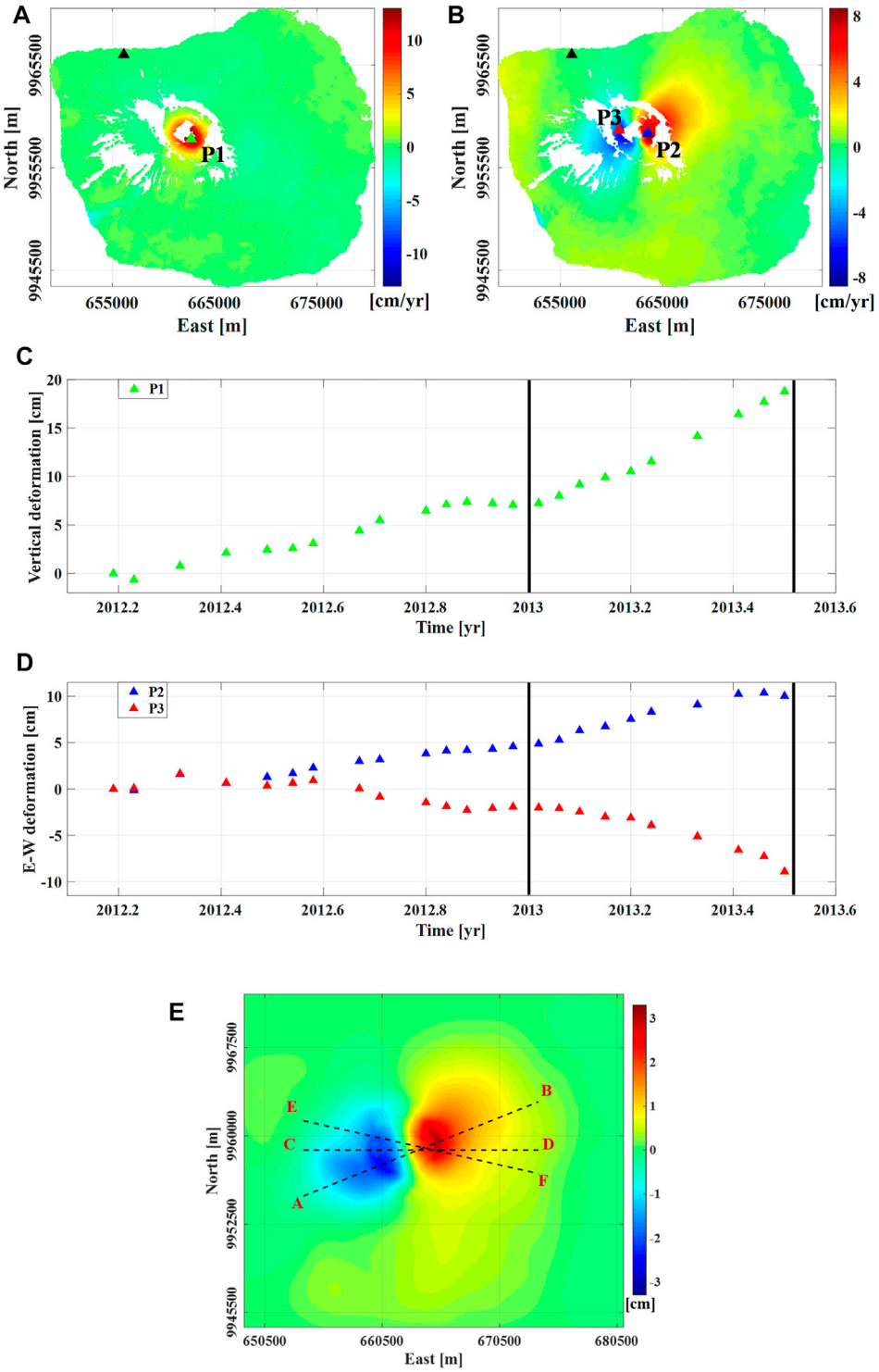

FIGURE 8 | DInSAR measurements at Fernandina volcano. The mean **(A)** vertical and **(B)** E-W velocity related to the time interval 2012–2013.5; black triangles indicate the reference pixel, while the green, blue, and red triangles the location of P1, P2, and P3 pixels, respectively. **(C)** Vertical and **(D)** E-W components of the deformation measured during the 2012–2013.5 time interval at P1 and P2-P3 pixels, respectively; black vertical continuous lines represent the selected temporal period. **(E)** Cumulative E-W deformation referred to the 1.5 km a.s.l. scale and recorded in the time interval 01/2013–06/2013. UTM-WGS84 projection zone: 15S.

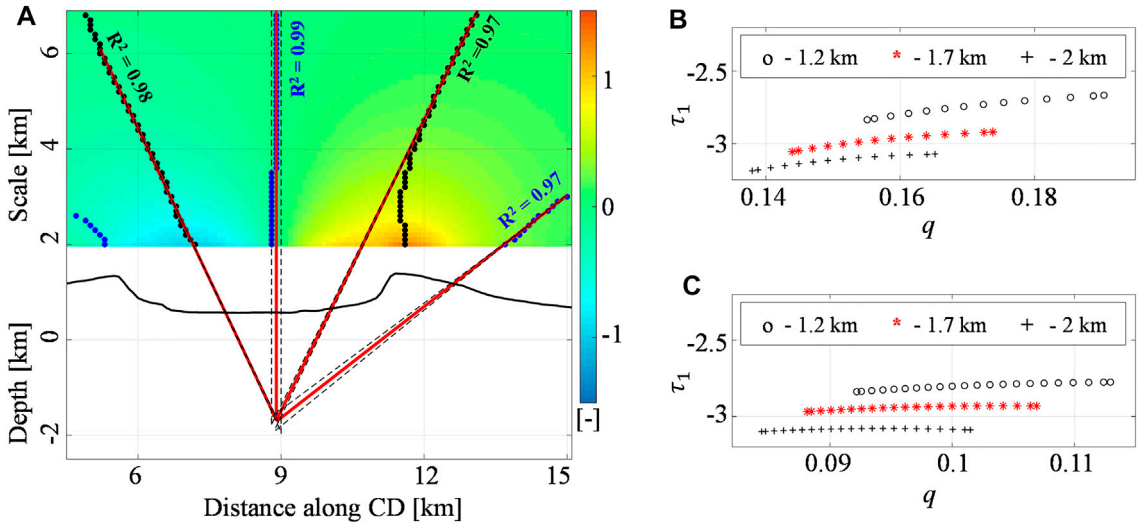

FIGURE 9 | Fernandina volcano: the first-order vertical derivative of E-W deformation. **(A)** The Multiridge method along the CD section of the first-order (p = 1) vertical derivative of the E-W component recorded in the time interval 01/2013–06/2013; blue and black dots point out the zeros of vertical (subset I) and horizontal (subset II) derivatives of the analyzed dataset, respectively. Vertical derivatives are also shown at different scales z; red solid and black dashed lines represent the best-fit regression lines and the linear regression boundary solutions, respectively. For each regression line, we indicate the R^2 coefficient; black solid lines represent the topography. **(B,C)** The ScalFun results; red stars and black crosses and circles indicate $\tau_1 = \partial \log f_1 / \partial \log z$ [-] in function of $q = 1/z$ [km^{-1}] calculated using the best-fit and boundary depth solutions retrieved by the Multiridge method, respectively, where f_1 are the values of the analyzed first-order vertical derivative at subset II.

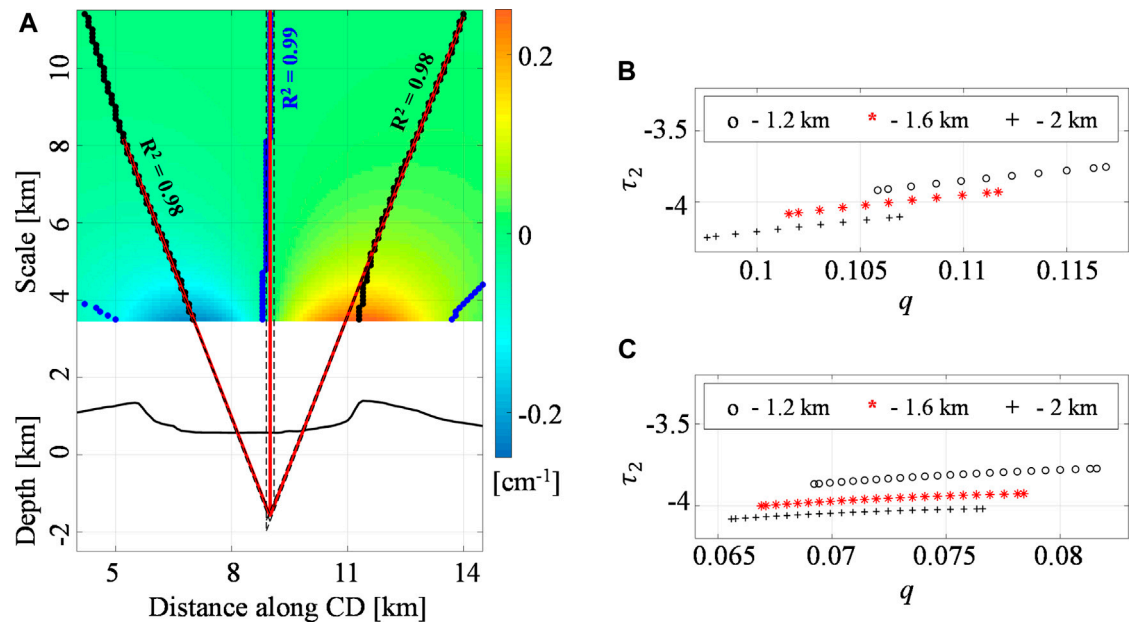

FIGURE 10 | Fernandina volcano: the second-order vertical derivative of E-W deformation. **(A)** The Multiridge method along the CD section of the second-order (p = 2) vertical derivative of the E-W component recorded in the time interval 01/2013–06/2013; blue and black dots point out the zeros of vertical (subset I) and horizontal (subset II) derivatives of the analyzed dataset, respectively. Vertical derivatives are also shown at different scales z; red solid and black dashed lines represent the best-fit regression lines and the linear regression boundary solutions, respectively. For each regression line, we indicate the R^2 coefficient; black solid lines are the topography. **(B,C)** The ScalFun results; red stars and black crosses and circles indicate $\tau_2 = \partial \log f_2 / \partial \log z$ [-] in function of $q = 1/z$ [km^{-1}] calculated using the best-fit and boundary depth solutions retrieved by the Multiridge method, respectively, where f_2 are the values of the analyzed second-order vertical derivative at subset II.

(662700 E ± 100 m, 9958800 N m) with 1.7 ± 0.4 km b.s.l. depth (**Figure 9A**). We apply the ScalFun method to both the left and right multiridge subset II by characterizing the solution with $N \sim 3$, since $\tau_1 \sim -3$ and $n \sim -2$ (**Figures 9B,C**), according to **Eqs 22**, **23**, **25** and $p = 1$. Then, we analyze the second-order vertical derivative, where the ridges intersection along the CD

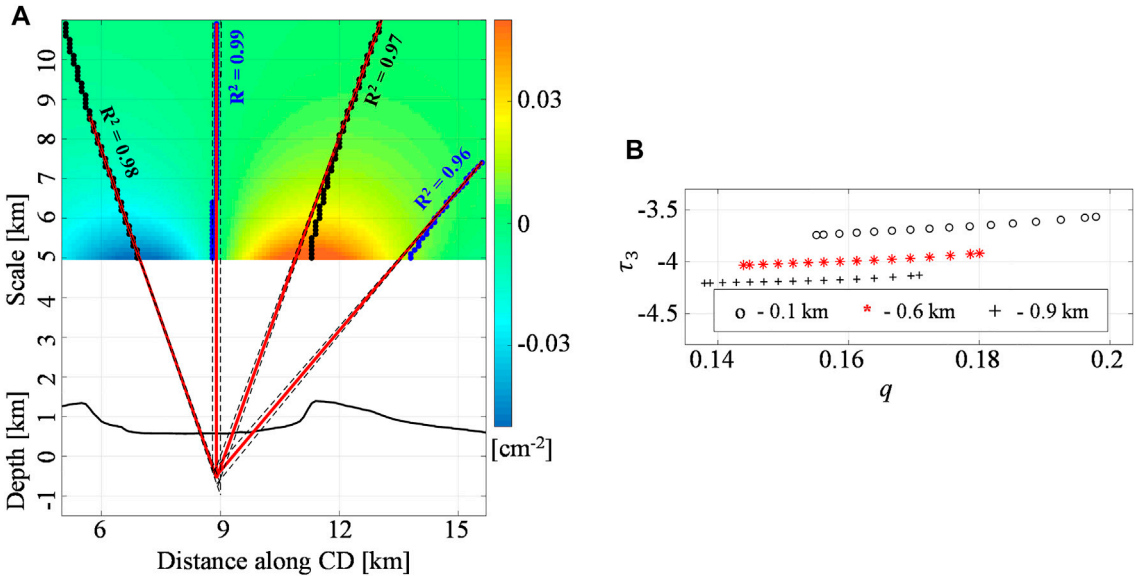

FIGURE 11 | Fernandina volcano: the third-order vertical derivative of E-W deformation. **(A)** The Multiridge method along the CD section of the third-order (p = 3) vertical derivative of the E-W component recorded in the time interval 01/2013–06/2013; blue and black dots point out the zeros of vertical (subset I) and horizontal (subset II) derivatives of the analyzed dataset, respectively. Vertical derivatives are also shown at different scales z; red solid and black dashed lines represent the best-fit regression lines and the linear regression boundary solutions, respectively. For each regression line, we indicate the R^2 coefficient; black solid lines represent the topography. **(B)** The ScalFun results; red stars and black crosses and circles indicate $\tau_3 = \partial \log f_3 / \partial \log z$ [-] in function of $q = 1/z$ [km^{-1}] calculated using the best-fit and boundary depth solutions retrieved by the Multiridge method, respectively, where f_3 are the values of the analyzed third-order vertical derivative at subset II.

TABLE 2 | Source solutions for Fernandina volcano retrieved in this study. p [-] and N [-] represent the order of the analyzed dataset and the structural index parameter, respectively. Depths are b.s.l.

Profile	p	East (km)	North (km)	Depth (km)	N
AB	1	662.8 ± 0.2	9958.5 ± 0.2	1.6 ± 0.3	3
	2	662.8 ± 0.2	9958.5 ± 0.2	1.6 ± 0.4	3
	3	662.8 ± 0.2	9958.5 ± 0.2	0.5 ± 0.3	2
CD	1	662.7 ± 0.1	9958.8	1.7 ± 0.4	3
	2	662.8 ± 0.1	9958.8	1.6 ± 0.4	3
	3	662.7 ± 0.1	9958.8	0.6 ± 0.5	2
EF	1	662.7 ± 0.2	9959.3 ± 0.1	1.7 ± 0.5	3
	2	662.5 ± 0.2	9959.3 ± 0.1	1.6 ± 0.4	3
	3	662.5 ± 0.2	9959.3 ± 0.1	0.6 ± 0.5	2

profile occurs at the point with coordinates 662800 E ± 100 m, 9958800 N m at 1.6 ± 0.4 km b.s.l. depth (**Figure 10A**). This source is characterized by $N \sim 3$ since $\tau_2 \sim -4$ and $n \sim -2$ (**Figures 10B,C**), according to **Eqs 22**, **23**, **25** and $p = 2$. Finally, we consider the third-order vertical derivative along the CD profile and retrieve an intersection located at 662700 E ± 100 m and 9958800 N m with 0.6 ± 0.5 km b.s.l. depth (**Figure 11A**). We describe this solution with $N \sim 2$, since $\tau_3 \sim -4$ and $n \sim -1$ (**Figure 11B**), according to **Eqs 22**, **23**, **25** and $p = 3$.

We carry out the analogous analyses by considering the other AB and EF profiles, which results for each order p are shown in **Supplementary Figures S4–S6**. **Supplementary Figure S7** shows a 3D plot of all the retrieved ridges intersections.

We summarize the retrieved results in **Table 2**.

4 DISCUSSION

In this work, we use the multi-scale approach to analyze DInSAR measurements and model the deformation sources in several volcanic environments. The proposed procedure is based on the harmonic and homogeneous properties of the deformation field, which has to satisfy Laplace's equation and the homogeneity law. In these conditions, we employ the Multiridge and ScalFun methods to retrieve the unconstrained geometrical information, such as the depth, the horizontal position, and the morphological features, by considering the properties of point-spherical, pipe-, and sill-like ideal sources. Despite some limitations affecting the multi-scale approach, it represents an alternative strategy with respect to the classical optimization/inverse methods since its solutions do not depend on a priori constraints of model parameters.

In this section, we will discuss the validity of the proposed multi-scale approach through: (1) theoretical argumentations, (2) application to synthetic deformation fields, and (3) different real cases.

4.1 Theory and Methods

We focus on the conditions for which the pressurized volcanic bodies generate a harmonic and homogeneous ground deformation field. In this framework, we show that Laplace's equation and the homogeneity law are surely

satisfied in the case of hydrostatically pressurized sources embedded in a homogeneous elastic half-space. It is well-known that these conditions are just an approximation of the real volcanic scenario (e.g., Gudmundsson, 2006; Hickey et al., 2016), as well as the case of many AMs. One of these is the Mogi model (Mogi, 1958). Its analytical expression is represented by the gradient of a Newtonian potential in the form $\phi = 1/r$ (Castaldo et al., 2018), which is a harmonic and homogeneous function. However, the multi-scale approach is also appropriate to model some classes of nonharmonic fields. Indeed, Castaldo et al. (2018) have applied this methodology to the deformation fields generated by spherical sources embedded in a heterogeneous and layered elastic half-space by retrieving negligible errors on the estimated parameters. Also, in this work, we propose the layered half-space model setting by considering a different source, represented by a sill-like one.

Here, we show that the proposed multi-scale strategy is based on two methods: The Multiridge method provides information on the center of deformation sources by evaluating the ridges intersection, which can also occur, for the pipes, sills, and dykes, at their top and/or boundaries. The ScalFun method characterizes the source shape through the estimates of the structural index N. For example, with $N \sim 3$, we are analyzing the fields generated by a mathematically equivalent body concentrated in its center, while $N \sim 2$ characterizes the pipe-like sources and ridges intersections related to their top. $N \sim 1$ is finally related to the edges or top vertexes of the planar bodies, such as sills- and dykes-like sources (e.g., Reid et al., 1990; Florio et al., 2014). We remark that these methods are based on the properties of continuous harmonic and homogeneous functions. The applicability depends evidently on the 2D distribution of deformation measurements, which should be spatially dense, and this occurs with the DInSAR dataset. On the contrary, the Leveling and Global Navigation Satellite System (GNSS) data generally lead to unreliable interpretation of the multi-scale results.

4.2 Application to Synthetic Tests

We perform several tests on the simulated harmonic and homogeneous fields. In particular, we analyze the vertical and E-W deformation components. Although the simulated N-S one should be available, we do not consider it since this study is conceived for the analysis of DInSAR measurements, which do not provide this information, due to the near-polar orbit of the SAR sensors. However, the harmonic and homogeneous properties of the deformation field also allow the involvement of the LOS components in the framework of the multi-scale procedure (Castaldo et al., 2018). In addition to the field component, we employ their vertical differentiations of order p since the harmonic properties allow us to compute them in the wavenumber domain. This operator increases the analysis resolution by emphasizing the signals high-wavenumber contributions that are related to the shallowest features of the sources, as the pipe's top and the sill's edges. It is important to note that the vertical differentiation also enhances the high-wavenumber noise of the dataset, which affect the lower scales. Therefore, when the signal-to-noise ratio is low, it is recommendable to perform the multi-scale analysis at rather large scales (Fedi et al., 2009). The scale-invariance vs. p is a property of the harmonic and homogeneous fields and, by using the vertical differentiation operator, we can verify this condition. The sphere test (I) represents the simplest example of this property, where both for the field components (vertical and E-W) and for their vertical derivative analysis, we observe ridges converging to the center of the body, with the structural index $N \sim 3$. Differently from the previous source, the pipe case (II) shows that the ridges at larger scales converge to the source center with $N \sim 3$, while at lower scales, they tend to intersect at its top (shallowest singular point). Accordingly, the vertical derivative analysis shows a ridges intersection nearby its top with $N \sim 2$. The N estimates and the related depths of each ridges intersection (center and top) allow us to interpret the responsible source as a vertically elongated one (e.g., pipe-like). Similarly, in the sill test (III), the ridges at larger scales intersect at the source center finding $N \sim 3$, while at lower scales, they are strongly influenced by the body edges. Indeed, by analyzing the vertical derivative of the field components, we retrieve the ridges intersections nearby the prism edges, with $N \sim 1$. We can correctly interpret the deformations generated by a planar body (e.g., sill-like).

It is worth noting that our simulations have shown that the Multiridge and ScalFun methods are valid tools to study the harmonic deformation fields of homogeneous sources. They have provided, in the worst cases, estimates on the depth to the source center affected by ~ 7% error with respect to the real value and on its top/edge position with 4% of error with respect to the source extent. The retrieved errors in controlled conditions may mainly depend on the replication of the harmonic field properties and the data sampling.

We obtain comparable errors on source parameters by analyzing the nonharmonic fields, generated by a sill embedded in a layered half-space (IV) and with the same random noise (V). In both the simulations, we retrieve the source depth to the center with only 5% error with respect to the expected values. This finding demonstrates that the Multiridge and ScalFun methods in the same conditions can be extended to the analysis of nonharmonic fields, as in the case of layered heterogeneous medium with weak physical parameters contrasts. Furthermore, we observe that the noisy dataset does not affect the multi-scale results, at least for the source center estimate.

Finally, with the last test (VI), we show the flexibility of the proposed methodology, which can be also used to analyze a multi-source scenario. This occurs by exploiting the vertical derivatives of the field that allow us to detect the parameters of both the modeled sources, with a maximum estimated error of 10% at the depth to the center.

4.3 Application to Real Cases

We use the Multiridge and ScalFun methods for analyzing three different American volcanoes. We show the applicability of the multi-scale approach in different volcanic environments, since

TABLE 3 | Source locations for Okmok volcano. Depths are b.s.l.

Study	Period	East (km)	North (km)	Depth (km)	Source type
Lu et al., (2005)	1992–2003	690.55	5923.85	3.2	Mogi model
Masterlark et al., (2010)	1995–2007	690.72	5923.98	3.1	Spherical
Biggs et al., (2010)	1992–2008	690.30	5923.60	3.4	Mogi model
Masterlark et al., (2012)	1995–1997	690.70	5923.91	3.5	Spherical
Castaldo et al., (2018)	2003–2004	690.90	5924.00	3.4	Spherical
Xue et al., (2020)	1997–2008	~	~	3.2	Mogi model
This study	2003–2004	691.00	5924.00	3.1	3D finite

TABLE 4 | Source locations for Fernandina volcano. Depths are b.s.l.

Study	Period/eruption	Depth (km)	Type
Jonsson et al., (1999)	1995 (lateral intrusion)	0–0.5	Rectangular dislocation
Chadwick et al., (2011)	2005 Pre-eruptive	0.9	Sill-like source
	(lateral intrusion)	6	Point source
	2005 Posteruptive	1.1	Sill-like source
	(lateral intrusion)	3.9	Point source
Bagnardi and Amelung, (2012)	2003–2010	1	Horizontal sill
	(lateral intrusion)	4.5	Horizontal sill
Bagnardi et al., (2013)	1995 (lateral intrusion)	1	Planar source
		1	Sill-like source
		5	Sill-like source
	2005 (lateral intrusion)	1	Sill-like source
	2009 (lateral intrusion)	5	Sill-like source
Pepe et al., (2017)	2012–2013 (summit caldera unrest)	1.5	Pipe-like source
This study	2013 (summit caldera unrest)	1.7	Pipe-like source

the same geodynamics settings and geochemical features do not characterize the considered systems.

Unlike the previous synthetic cases, we evaluate R^2 parameter for each ridge and the related intersection uncertainties, since different signal contributions (i.e., instrumental/experimental errors, high-wavenumber noise in the dataset, effect due to the draped-to-flat upward continuation at the areas with high slopes, and effects due to other nonvolcanic sources), can affect the multi-scale results. We can avoid some of these contributions that are predominant at the lower scales by focusing the analysis on the rather larger scales of the multi-scale dataset.

We perform the first application at Uturuncu volcano (Bolivia), which is located on the largest updoming zones on the Earth. In this framework, it is well known that the deep APMB source has a crucial role for the observed multi-decade decimeter-scale deformation signal (Allmendinger et al., 1997; Schmitz et al., 1997; Schilling et al., 1997; Chmielowski et al., 1999; Pritchard and Simons, 2002; Zandt et al., 2003; Pritchard and Simons, 2004; Sparks et al., 2008; Fialko and Pearse, 2012; del Potro et al., 2013; Henderson and Pritchard, 2013; Hickey et al., 2013; Walter and Motagh, 2014; Ward et al., 2014; Comeau et al., 2015; Comeau et al., 2016; Perkins et al., 2016; Gottsmann et al., 2017; Kukarina et al., 2017; Ward et al., 2017; McFarlin et al., 2017; Henderson and Pritchard, 2017; Pritchard et al., 2018; Barone et al., 2019), despite the evidences of geophysical, seismological, and petrological data analyses also highlighting the hypothesis of shallow sources (Sparks et al., 2008; Jay et al., 2012; Muir et al., 2014; Alvizuri and Tape, 2016; Comeau et al., 2016; Lau et al., 2018; Barone et al., 2019). We study the cumulative vertical deformation related to the transient 2007 unrest, for which the AMPB is supposed to be not responsible of the observed ground deformation field (Barone et al., 2019). Our results infer the depth to the source center of 4.5 km b.s.l., with a structural index $N \sim 3$, pointing out the accordance with the supposed scenario of the existence of a shallow hydrothermal active system beneath Uturuncu volcano (e.g., Gottsmann et al., 2017; Lau et al., 2018). This also matches with the low resistivity zones, related to the saline fluids of the magmatic and/or meteoric origin (Comeau et al., 2015; Comeau et al., 2016), and with other geophysical and petrological data analysis (Sparks et al., 2008; Jay et al., 2012; Muir et al., 2014; Alvizuri and Tape, 2016). However, the multi-scale approach does not provide any information on the nature of the shallow source below Uturuncu volcano, for which the hypothesis of a hydrothermal system is still the most reliable option explaining the geophysical, seismological, and geodetic anomalies (Hudson et al., 2022).

We perform the second analysis at Okmok volcano (Alaska, United States), where the multi-scale approach has been already applied to the single LOS component. In this work, we consider the same dataset of Castaldo et al. (2018), but we apply the Multiridge and ScalFun methods to its second-order vertical derivative. Here, the higher resolution analysis shows the

scale-invariance vs. p. of the multi-scale results. Indeed, they do not significantly change by increasing p, we estimate the depth to the source center, with $N \sim 3$, at 3.1 km b.s.l. in the case of $p = 2$, which agrees with those obtained with $p = 0$ (3.4 km b.s.l. and $N \sim 3$). It follows that the analyzed dataset is in good approximation with the harmonic and homogeneous field, and the analyzed source consists of a 3D concentrated body. The retrieved source (**Table 3**) agrees with those proposed by several authors modeling the 1997–2008 intereruptive stage (e.g., Lu et al., 2005; Biggs et al., 2010; Masterlark et al., 2010; Masterlark et al., 2012; Xue et al., 2020), despite the fact that our analysis is related to a smaller time interval (2003–2004).

Finally, we apply the multi-scale methods to evaluate the depth, horizontal location, and morphological features of the deformation source related to the 2013 unrest at Fernandina volcano. Different from the previous real cases, we analyze the E-W deformation component. We specify that the coherent measurement points (**Figure 8A**) are not well distributed at the summit caldera (uncorrelated signals), where the maximum vertical deformation is expected. A better data distribution is observed at the volcano flanks, where the maxima and minima of the E-W deformation anomaly are located. Our findings point out two clusters of solutions with different N values and we associate both to a unique volcanic body. The deformation pattern is interpreted as generated by a vertically elongated source with 1.5–1.7 km b.s.l. depth to the center ($N \sim 3$) and 0.5–0.6 km b.s.l. depth to the top ($N \sim 2$). We specify that our findings are robust and give recurring solutions by analyzing different profiles and different p-order cases. We compare them with the geodetic studies based on the optimization/inverse methods (**Table 4**), finding that the suggested volcanic source is compatible with the scenario of Bagnardi and Amelung (2012), where the magmatic feeding system consists of connected deep and shallow sill-like reservoirs. Our vertical source just images a conduit body for magma or fluid ascent from the deeper to shallower portions of the volcanic system. The retrieved results also agree with the pipe-like source proposed by Pepe et al. (2017). However, we note that our and latter works refer to the modeling of uplift that has involved the central part of the summit caldera. Instead, Bagnardi and Amelung (2012) have mainly investigated the unrest events that have led to the intrusion of lateral dykes (Jonsson et al., 1999; Chadwick et al., 2011).

4.4 Concluding Remarks

We conclude the work by listing the main features of the proposed multi-scale approach.

The methodology represents an alternative procedure with respect to the optimization/inverse methods, which, differently from our approach, generally need to fix information, such as the medium elastic parameters, the source physical parameters, and its geometry.

The methods provide an unconstrained source geometrical model, while they do not provide information on the source physical parameters. Their results can also be used as constraints for the inverse/optimization modeling procedures, aiming at estimating a more complete set of source parameters.

The methods are suitable to:

- Analyze any deformation components;
- Perform high-resolution analyses by using the vertical differentiation operator;
- Model multi-source cases;

and their results:

- Do not depend on lower variations of the physical parameters of the elastic half-space;
- Are stable *vs.* noise.

Although the presented multi-scale approach is restricted to the analysis of sources as point-spherical, pipe-, and sill-like ones, future developments will concern the use of Multiridge and ScalFun methods in the case of sources with complex geometry.

DATA AVAILABILITY STATEMENT

The data analyzed in this study is subject to the following licenses/restrictions: The datasets can be accessed by contacting the corresponding author. Requests to access these datasets should be directed to castaldo.r@irea.cnr.it.

AUTHOR CONTRIBUTIONS

AB: validation, writing the original draft. MF: supervision, review and editing. SP: data curation. GS: data curation, review and editing. PT: supervision, review and editing. RC: conceptualization, supervision, review and editing.

FUNDING

This work has been supported by the projects DTA.AD003.433—PRIN 2017—FLUIDs and DTA.AD004.286 "Accordo 2019–2021 Dipartimento Protezione Civile e CNR—IREA".

ACKNOWLEDGMENTS

We would like to thank the Editor and the reviewers for critically reviewing the manuscript and providing valuable comments to improve the quality of the manuscript.

SUPPLEMENTARY MATERIAL

The Supplementary Material for this article can be found online at: https://www.frontiersin.org/articles/10.3389/feart.2022.859479/full#supplementary-material

REFERENCES

Allmendinger, R. W., Jordan, T. E., Kay, S. M., and Isacks, B. L. (1997). The Evolution of the Altiplano-Puna Plateau of the central Andes. *Annu. Rev. Earth Planet. Sci.* 25, 139–174. doi:10.1146/annurev.earth.25.1.139

Alvizuri, C., and Tape, C. (2016). Full Moment Tensors for Small Events (Mw. *Geophys. J. Int.* 206, 1761–1783. doi:10.1093/gji/ggw247

Bagnardi, M., Amelung, F., and Poland, M. P. (2013). A New Model for the Growth of Basaltic Shields Based on Deformation of Fernandina Volcano, Galápagos Islands. *Earth Planet. Sci. Lett.* 377-378, 358–366. doi:10.1016/j.epsl.2013.07.016

Bagnardi, M., and Amelung, F. (2012). Space-geodetic Evidence for Multiple Magma Reservoirs and Subvolcanic Lateral Intrusions at Fernandina Volcano, Galápagos Islands. *J. Geophys. Res.* 117, B10406. doi:10.1029/2012JB009465

Barone, A., Fedi, M., Tizzani, P., and Castaldo, R. (2019). Multiscale Analysis of DInSAR Measurements for Multi-Source Investigation at Uturuncu Volcano (Bolivia). *Remote sensing* 11, 703. doi:10.3390/rs11060703

Battaglia, M., Cervelli, P. F., and Murray, J. R. (2013). dMODELS: A MATLAB Software Package for Modeling Crustal Deformation Near Active Faults and Volcanic Centers. *J. Volcanology Geothermal Res.* 254, 1–4. doi:10.1016/j.jvolgeores.2012.12.018

Battaglia, M., Gottsmann, J., Carbone, D., and Fernández, J. (2008). 4D Volcano Gravimetry. *Geophysics* 73, WA3–WA18. doi:10.1190/1.2977792

Biggs, J., Lu, Z., Fournier, T., and Freymueller, J. T. (2010). Magma Flux at Okmok Volcano, Alaska, from a Joint Inversion of Continuous GPS, Campaign GPS, and Interferometric Synthetic Aperture Radar. *J. Geophys. Res.* 115, B12401. doi:10.1029/2010JB007577

Blakely, J. R. (1996). *Potential Theory in Gravity and Magnetic Applications*. revised ed. Cambridge: Cambridge University Press.

Bonaccorso, A., and Davis, P. M. (1999). Models of Ground Deformation from Vertical Volcanic Conduits with Application to Eruptions of Mount St. Helens and Mount Etna. *J. Geophys. Res.* 104 (B5), 10531–10542. doi:10.1029/1999JB900054

Castaldo, R., Barone, A., Fedi, M., and Tizzani, P. (2018). Multiridge Method for Studying Ground-Deformation Sources: Application to Volcanic Environments. *Sci. Rep.* 8, 13420. doi:10.1038/s41598-018-31841-4

Castaldo, R., Tizzani, P., and Solaro, G. (2021). Inflating Source Imaging and Stress/Strain Field Analysis at Campi Flegrei Caldera: The 2009-2013 Unrest Episode. *Remote Sensing* 13 (12), 2298. doi:10.3390/rs13122298

Chadwick, W. W., Jónsson, S., Geist, D. J., Poland, M., Johnson, D. J., Batt, S., et al. (2011). The May 2005 Eruption of Fernandina Volcano, Galápagos: The First Circumferential dike Intrusion Observed by GPS and InSAR. *Bull. Volcanol.* 73 (6), 679–697. doi:10.1007/s00445-010-0433-0

Chmielowski, J., Zandt, G., and Haberland, C. (1999). The Central Andean Altiplano-Puna Magma Body. *Geophys. Res. Lett.* 26 (6), 783–786. doi:10.1029/1999GL900078

Comeau, M. J., Unsworth, M. J., and Cordell, D. (2016). New Constraints on the Magma Distribution and Composition beneath Volcán Uturuncu and the Southern Bolivian Altiplano from Magnetotelluric Data. *Geosphere* 12 (5), 1391–1421. doi:10.1130/GES01277.1

Comeau, M. J., Unsworth, M. J., Ticona, F., and Sunagua, M. (2015). Magnetotelluric Images of Magma Distribution beneath Volcán Uturuncu, Bolivia: Implications for Magma Dynamics. *Geology* 43 (3), 243–246. doi:10.1130/G36258.1

Corbi, F., Rivalta, E., Pinel, V., Maccaferri, F., Bagnardi, M., and Acocella, V. (2015). How Caldera Collapse Shapes the Shallow Emplacement and Transfer of Magma in Active Volcanoes. *Earth Planet. Sci. Lett.* 431, 287–293. doi:10.1016/j.epsl.2015.09.028

de Silva, S. L., and Gosnold, W. D. (2007). Episodic Construction of Batholiths: Insights from the Spatiotemporal Development of an Ignimbrite Flare-Up. *J. Volcanology Geothermal Res.* 167, 320–335. doi:10.1016/j.jvolgeores.2007.07.015

del Potro, R., Díez, M., Blundy, J., Camacho, A. G., and Gottsmann, J. (2013). Diapiric Ascent of Silicic Magma beneath the Bolivian Altiplano. *Geophys. Res. Lett.* 40, 2044–2048. doi:10.1002/grl.50493

Dieterich, J. H., and Decker, R. W. (1975). Finite Element Modeling of Surface Deformation Associated with Volcanism. *J. Geophys. Res.* 80 (29), 4094–4102. doi:10.1029/jb080i029p04094

Dzurisin, D. (2007). *Volcano Deformation, Geodetic Monitoring Techniques*. New York: Springer.

Fedi, M. (2007). DEXP: A Fast Method to Determine the Depth and the Structural index of Potential fields Sources. *Geophysics* 72 (1), I1–I11. doi:10.1190/1.2399452

Fedi, M., Florio, G., and Paoletti, V. (2015). MHODE: a Local-Homogeneity Theory for Improved Source-Parameter Estimation of Potential fields. *Geophys. J. Int.* 202, 887–900. doi:10.1093/gji/ggv185

Fedi, M., Florio, G., and Quarta, T. A. (2009). Multiridge Analysis of Potential fields: Geometric Method and Reduced Euler Deconvolution. *Geophysics* 74 (4), L53–L65. doi:10.1190/1.3142722

Fialko, Y., Khazan, Y., and Simons, M. (2001). Deformation Due to a Pressurized Horizontal Circular Crack in an Elastic Half-Space, with Applications to Volcano Geodesy. *Geophys. J. Int.* 146, 181–190. doi:10.1046/j.1365-246x.2001.00452.x

Fialko, Y., and Pearse, J. (2012). Sombrero Uplift above the Altiplano-Puna Magma Body: Evidence of a Ballooning Mid-crustal Diapir. *Science* 338, 6104250–6104252. doi:10.1126/science.1226358

Finney, B., Turner, S., Hawkesworth, C., Larsen, J., Nye, C., George, R., et al. (2008). Magmatic Differentiation at an Island-Arc Caldera: Okmok Volcano, Aleutian Islands, Alaska. *J. Petrol.* 49 (5), 857–884. doi:10.1093/petrology/egn008

Florio, G., Fedi, M., and Pašteka, R. (2014). On the Estimation of the Structural index from Low-Pass Filtered Magnetic Data. *Geophysics* 79 (6), J67–J80. doi:10.1190/geo2013-0421.1

Geerstma, J., and Van Opstal, K. (1973). A Numerical Technique for Predicting Subsidence above Compacting Reservoirs, Based on the Nucleus of Strain Concept. *Verhandelingen Kon. Ned. Geol. Mijnbouwk. Gen.* 28, 63

Gottsmann, J., Blundy, J., Henderson, S., Pritchard, M. E., and Sparks, R. S. J. (2017). Thermomechanical Modeling of the Altiplano-Puna Deformation Anomaly: Multiparameter Insights into Magma Mush Reorganization. *Geosphere* 13, GES014201. doi:10.1130/GES01420.1

Gudmundsson, A. (2006). How Local Stresses Control Magma-Chamber Ruptures, Dyke Injections, and Eruptions in Composite Volcanoes. *Earth-Science Rev.* 79 (1-2), 1–31. doi:10.1016/j.earscirev.2006.06.006

Henderson, S. T., and Pritchard, M. E. (2013). Decadal Volcanic Deformation in the Central Andes Volcanic Zone Revealed by InSAR Time Series. *Geochem. Geophys. Geosyst.* 14 (5), 1358–1374. doi:10.1002/ggge.20074

Henderson, S. T., and Pritchard, M. E. (2017). Time-dependent Deformation of Uturuncu Volcano, Bolivia, Constrained by GPS and InSAR Measurements and Implications for Source Models. *Geosphere* 13 (6), 1834–1854. doi:10.1130/GES01203.1

Hickey, J., Gottsmann, J., and del Potro, R. (2013). The Large-Scale Surface Uplift in the Altiplano-Puna Region of Bolivia: A Parametric Study of Source Characteristics and Crustal Rheology Using Finite Element Analysis. *Geochem. Geophys. Geosyst.* 14 (3), 540–555. doi:10.1002/ggge.20057

Hickey, J., Gottsmann, J., Nakamichi, H., and Iguchi, M. (2016). Thermomechanical Controls on Magma Supply and Volcanic Deformation: Application to Aira Caldera, Japan. *Sci. Rep.* 6, 32691. doi:10.1038/srep32691

Hudson, T. S., Kendall, J.-M., Pritchard, M. E., Blundy, J. D., and Gottsmann, J. H. (2022). From Slab to Surface: Earthquake Evidence for Fluid Migration at Uturuncu Volcano, Bolivia. *Earth Planet. Sci. Lett.* 577, 117268. doi:10.1016/j.epsl.2021.117268

Jay, J. A., Pritchard, M. E., West, M. E., Christensen, D., Haney, M., Minaya, E., et al. (2012). Shallow Seismicity, Triggered Seismicity, and Ambient Noise Tomography at the Long-Dormant Uturuncu Volcano, Bolivia. *Bull. Volcanol* 74, 817–837. doi:10.1007/s00445-011-0568-7

Jónsson, S., Zebker, H., Cervelli, P., Segall, P., Garbeil, H., Mouginis-Mark, P., et al. (1999). A Shallow-Dipping dike Fed the 1995 Flank Eruption at Fernandina Volcano, Galápagos, Observed by Satellite Radar Interferometry. *Geophys. Res. Lett.* 26 (8), 1077–1080. doi:10.1029/1999GL900108

Kukarina, E., West, M., Keyson, L. H., Koulakov, I., Tsibizov, L., and Smirnov, S. (20172017). Focused Magmatism beneath Uturuncu Volcano, Bolivia: Insights from Seismic Tomography and Deformation Modeling. *Geosphere* 13 (6), 1855–1866. doi:10.1130/GES01403.1

Lau, N., Tymofyeyeva, E., and Fialko, Y. (2018). Variations in the Long-Term Uplift Rate Due to the Altiplano-Puna Magma Body Observed with Sentinel-1 Interferometry. *Earth Planet. Sci. Lett.* 491, 43–47. doi:10.1016/j.epsl.2018.03.026

Love, A. E. H. (1906). *A Treatise on the Mathematical Theory of Elasticity*. second ed. Cambridge: Cambridge University Press.

Lu, Z., Masterlark, T., and Dzurisin, D. (2005). Interferometric Synthetic Aperture Radar Study of Okmok Volcano, Alaska, 1992-2003: Magma Supply Dynamics and Postemplacement Lava Flow Deformation. *J. Geophys. Res.* 110, B02403. doi:10.1029/2004JB003148

Masterlark, T., Feigl, K. L., Haney, M., Stone, J., Thurber, C., and Ronchin, E. (2012). Nonlinear Estimation of Geometric Parameters in FEMs of Volcano Deformation: Integrating Tomography Models and Geodetic Data for Okmok Volcano, Alaska. *J. Geophys. Res.* 117, a–n. doi:10.1029/2011JB008811

Masterlark, T., Haney, M., Dickinson, H., Fournier, T., and Searcy, C. (2010). Rheologic and Structural Controls on the Deformation of Okmok Volcano, Alaska: FEMs, InSAR, and Ambient Noise Tomography. *J. Geophys. Res.* 115, B02406. doi:10.1029/2009JB006324

McBirney, A. R., and Williams, H. (1969). Geology and Petrology of the Galápagos Islands. *Geol. Soc. Am. Mem.* 118, 1–197. doi:10.1130/mem118-p1

McFarlin, H., Christensen, D., McNutt, S. R., Ward, K. M., Ryan, J., Zandt, G., et al. (2017). Receiver Function Analyses of Uturuncu Volcano, Bolivia and Vicinity. *Geosphere* 14 (1), 50–64. doi:10.1130/GES01560.1

McTigue, D. F. (1987). Elastic Stress and Deformation Near a Finite Spherical Magma Body: Resolution of the point Source Paradox. *J. Geophys. Res.* 92 (B12), 12931–12940. doi:10.1029/JB092iB12p12931

Milano, M., Fedi, M., and Fairhead, J. D. (2016). The Deep Crust beneath the Trans-European Suture Zone from a Multiscale Magnetic Model. *J. Geophys. Res. Solid Earth* 121, 6276–6292. doi:10.1002/2016JB012955

Mogi, K. (1958). *Relation between Eruptions of Various Volcanoes and the Deformations of Ground Surfaces Around Them*, 36. Tokyo: Bullettin of the Earthquake Research Institute, University of Tokio, 99–134.

Muir, D. D., Blundy, J. D., Rust, A. C., and Hickey, J. (2014). Experimental Constraints on Dacite Pre-eruptive Magma Storage Conditions beneath Uturuncu Volcano. *J. Petrol.* 55 (4), 749–767. doi:10.1093/petrology/egu005

Okada, Y. (1985). Surface Deformation Due to Shear and Tensile Faults in a Half-Space. *Bullettin Seismological Soc. America* 75 (4), 1135–1154. doi:10.1785/bssa0750041135

Olmsted, J. M. A. (1961). *Advanced Calculus*. first ed. New York: Prentice-Hall PTR.

Paoletti, V., Milano, M., Baniamerian, J., and Fedi, M. (2020). Magnetic Field Imaging of Salt Structures at Nordkapp Basin, Barents Sea. *Geophys. Res. Lett.* 47, e2020GL089026. doi:10.1029/2020GL089026

Pepe, S., Castaldo, R., De Novellis, V., D'Auria, L., De Luca, C., Casu, F., et al. (2017). New Insights on the 2012-2013 Uplift Episode at Fernandina Volcano (Galápagos). *Geophys. J. Int.* 211, 673–685. doi:10.1093/gji/ggx330

Pepe, S., De Siena, L., Barone, A., Castaldo, R., D'Auria, L., Manzo, M., et al. (2019). Volcanic Structures Investigation through SAR and Seismic Interferometric Methods: The 2011-2013 Campi Flegrei Unrest Episode. *Remote Sensing Environ.* 234, 111440. doi:10.1016/j.rse.2019.111440

Perkins, J. P., Ward, K. M., de Silva, S. L., Zandt, G., Beck, S. L., and Finnegan, N. J. (2016). Surface Uplift in the Central Andes Driven by Growth of the Altiplano Puna Magma Body. *Nat. Commun.* 7, 13185. doi:10.1038/ncomms13185

Pritchard, M. E., de Silva, S. L., Michelfelder, G., Zandt, G., McNutt, S. R., Gottsmann, J., et al. (2018). Synthesis: PLUTONS: Investigating the Relationship between Pluton Growth and Volcanism in the Central Andes. *Geosphere* 14 (3), 954–982. doi:10.1130/GES01578.1

Pritchard, M. E., and Simons, M. (2002). A Satellite Geodetic Survey of Large-Scale Deformation of Volcanic Centres in the central Andes. *Nature* 418, 167–171. doi:10.1038/nature00872

Pritchard, M. E., and Simons, M. (2004). Surveying Volcanic Arcs with Satellite Radar Interferometry: The Central Andes, Kamchatka, and beyond. *GSA Today* 14, 8. doi:10.1130/1052-5173(2004)014<4:svawsr>2.0.co;2

Reid, A. B., Allsop, J. M., Granser, H., Millett, A. J., and Somerton, I. W. (1990). Magnetic Interpretation in Three Dimensions Using Euler Deconvolution. *Geophysics* 55 (1), 80–91. doi:10.1190/1.1442774

Ridsdill-Smith, T. A., and Dentith, M. C. (1999). The Wavelet Transform in Aeromagnetic Processing. *Geophysics* 64 (4), 1003–1013. doi:10.1190/1.1444609

Rodríguez-Molina, S., González, P. J., Charco, M., Negredo, A. M., and Schmidt, D. A. (2021). Time-Scales of Inter-eruptive Volcano Uplift Signals: Three Sisters Volcanic Center, Oregon (United States). *Front. Earth Sci.* 8 (645), 1–30. doi:10.3389/feart.2020.577588

Sadd, M. H. (2005). *Elasticity Theory, Applications, and Numerics*. USA: Elsevier.

Schilling, F. R., Partzsch, G. M., Brasse, H., and Schwarz, G. (1997). Partial Melting below the Magmatic Arc in the central Andes Deduced from Geoelectromagnetic Field Experiments and Laboratory Data. *Phys. Earth Planet. Interiors* 103, 17–31. doi:10.1016/S0031-9201(97)00011-3

Schmitz, M., Heinsohn, W.-D., and Schilling, F. R. (1997). Seismic, Gravity and Petrological Evidence for Partial Melt beneath the Thickened Central Andean Crust (21-23°S). *Tectonophysics* 270, 313–326. doi:10.1016/S0040-1951(96)00217-X

Sparks, R. S. J., Folkes, C. B., Humphreys, M. C. S., Barfod, D. N., Clavero, J., Sunagua, M. C., et al. (2008). Uturuncu Volcano, Bolivia: Volcanic Unrest Due to Mid-crustal Magma Intrusion. *Am. J. Sci.* 308, 727–769. doi:10.2475/06.2008.01

Sun, R. J. (1969). Theoretical Size of Hydraulically Induced Horizontal Fractures and Corresponding Surface Uplift in an Idealized Medium. *J. Geophys. Res.* 74, 5995–6011. doi:10.1029/JB074i025p05995

Tizzani, P., Battaglia, M., Castaldo, R., Pepe, A., Zeni, G., and Lanari, R. (2015). Magma and Fluid Migration at Yellowstone Caldera in the Last Three Decades Inferred from InSAR, Leveling, and Gravity Measurements. *J. Geophys. Res. Solid Earth* 120, 2627–2647. doi:10.1002/2014JB011502

Vitale, A., and Fedi, M. (2020). Self-constrained Inversion of Potential fields through a 3D Depth Weighting. *Geophysics* 85 (6), G143–G156. doi:10.1190/GEO2019-0812.1

Walter, T. R., and Motagh, M. (2014). Deflation and Inflation of a Large Magma Body beneath Uturuncu Volcano, Bolivia? Insights from InSAR Data, Surface Lineaments and Stress Modelling. *Geophys. J. Int.* 198, 462–473. doi:10.1093/gji/ggu080

Ward, K. M., Delph, J. R., Zandt, G., Beck, S. L., and Ducea, M. N. (2017). Magmatic Evolution of a Cordilleran Flare-Up and its Role in the Creation of Silicic Crust. *Sci. Rep.* 7, 90471–90478. doi:10.1038/s41598-017-09015-5

Ward, K. M., Zandt, G., Beck, S. L., Christensen, D. H., and McFarlin, H. (2014). Seismic Imaging of the Magmatic Underpinnings beneath the Altiplano-Puna Volcanic Complex from the Joint Inversion of Surface Wave Dispersion and Receiver Functions. *Earth Planet. Sci. Lett.* 404, 43–53. doi:10.1016/j.epsl.2014.07.022

Xue, X., Freymueller, J., and Lu, Z. (2020). Modeling the Posteruptive Deformation at Okmok Based on the GPS and InSAR Time Series: Changes in the Shallow Magma Storage System. *J. Geophys. Res. Solid Earth* 125, e2019JB017801. doi:10.1029/2019JB017801

Yang, X.-M., Davis, P. M., and Dieterich, J. H. (1988). Deformation from Inflation of a Dipping Finite Prolate Spheroid in an Elastic Half-Space as a Model for Volcanic Stressing. *J. Geophys. Res.* 93 (B5), 4249–4257. doi:10.1029/JB093iB05p04249

Zandt, G., Leidig, M., Chmielowski, J., Baumont, D., and Yuan, X. (2003). Seismic Detection and Characterization of the Altiplano-Puna Magma Body, Central Andes. *Pure Appl. Geophys.* 160, 789–807. doi:10.1007/PL00012557

Conflict of Interest: The authors declare that the research was conducted in the absence of any commercial or financial relationships that could be construed as a potential conflict of interest.

Publisher's Note: All claims expressed in this article are solely those of the authors and do not necessarily represent those of their affiliated organizations, or those of the publisher, the editors, and the reviewers. Any product that may be evaluated in this article, or claim that may be made by its manufacturer, is not guaranteed or endorsed by the publisher.